

Semiconductor Rydberg Physics

Marc Aßmann and Manfred Bayer *

This topical review addresses how semiconductor systems may reveal scalable properties similar to those known from Rydberg atoms and in which ways they may be utilized for precision sensing and to realize huge long-range interactions in semiconductor systems. Due to the interdisciplinary nature of the field, it has a twofold purpose: First, it may serve as an introduction to Rydberg physics for semiconductor physicists unfamiliar with the topic. Second, it may also serve as an overview of the specific opportunities and challenges arising in semiconductor physics for researchers who are familiar with Rydberg physics of cold atom gases, but new to the field of semiconductor physics. The review starts with an introduction on the general properties of excitons in semiconductors. Then, the material system Cu_2O , which is the best developed platform for semiconductor Rydberg physics at the moment, is discussed in detail.

1. Introduction

Rydberg atoms, where the outer electron is promoted to a highly excited state with huge principal quantum number n , show exaggerated and unique properties.^[1] These result in huge interactions and strong sensitivity to external fields, which is highly beneficial both for precision sensing and for realizing finely tunable atomic properties and interactions. In principle, any system with a Coulomb-bound electron will give rise to a Rydberg-like series of states and offers the potential to perform Rydberg physics. This includes atoms, ions, and molecules as well as excitons in semiconductor systems. However, most of the fundamental concepts have been demonstrated first in atomic systems. The reason for this is simple. Given that one only investigates a single atom species and isotope, all atoms are inherently identical. As uniformity of the systems of interest is a big issue for scalable quantum technologies ranging from quantum information^[2] to precision sensing of electromagnetic fields,^[3–5] Rydberg atoms are at a significant advantage with respect to complex composite or artificial

systems. Only recently it has been demonstrated that also semiconductor systems may become so pure that Rydberg physics is indeed observable.^[6]

In this review, we first give a brief overview on the general fundamentals of Rydberg physics and then discuss specifics of semiconductor-based implementations of Rydberg physics. We introduce typical material systems and how they differ from their atomic counterparts and provide a brief outlook on future perspectives.

2. Rydberg Physics

From a historical point of view, the first measurements of spectral lines go back to Ångström^[7] and his experimental findings were described theoretically first by Balmer^[8] and later in a more general and tractable form by Rydberg,^[9] which suggests that the binding energies of electronic states may be written in terms of the principal quantum number n as

$$E_n = -\frac{E_{\text{Ryd}}}{(n - \delta)^2}, \quad (1)$$

where E_{Ryd} denotes the Rydberg energy and δ represents the quantum defect. As a particular feature of Rydberg atoms, they are to first approximation hydrogen-like systems, which allows for a rather straightforward description of the physics involved. The Coulomb interaction energy between two elementary charges of opposite sign at a distance r is given by


$$E_C = -\frac{1}{4\pi\epsilon_0\epsilon_r} \frac{e^2}{r}, \quad (2)$$

where ϵ_r denotes the relative permittivity of the medium, in which the charges reside. For all systems where deviations from this ideal r^{-1} -dependence occur, for example due to screening, these deviations may be incorporated by using a non-zero value of the quantum defect δ . For an ideal Coulomb potential, one may directly determine the Rydberg energy of hydrogen-like systems to be

$$E_{\text{Ryd}} = \frac{\mu e^4}{32\epsilon_0^2 \epsilon_r^2 \pi^2 \hbar^2}, \quad (3)$$

where μ corresponds to the reduced mass of the two charges involved. This basic framework already allows one to estimate many properties of Rydberg systems. For example, the properties of the Rydberg states associated with the different quantum numbers show characteristic scaling laws with $n^{[1,10]}$: the mean

Prof. M. Aßmann, Prof. M. Bayer
Experimentelle Physik 2
Technische Universität Dortmund
Dortmund D-44221, Germany
E-mail: manfred.bayer@tu-dortmund.de

 The ORCID identification number(s) for the author(s) of this article can be found under <https://doi.org/10.1002/qute.201900134>

© 2020 The Authors. Published by WILEY-VCH Verlag GmbH & Co. KGaA, Weinheim. This is an open access article under the terms of the Creative Commons Attribution License, which permits use, distribution and reproduction in any medium, provided the original work is properly cited.

DOI: 10.1002/qute.201900134

separation between electron and nucleus and therefore also the dipole moment scales as n^2 , the natural line width of a Rydberg state scales as n^{-3} and its polarizability scales as n^7 . These characteristic scaling laws already imply that highly excited Rydberg states show exaggerated properties such as huge interactions between Rydberg atoms and enormous sensitivity to external fields. In detail, the interaction potential between two atoms at a separation R due to dipole–dipole interactions is given by

$$U_{\text{dd}} = \frac{C_3}{R^3}, \quad (4)$$

where C_3 scales as n^4 , while the van-der-Waals interaction potential

$$U_{\text{vdW}} = \frac{C_6}{R^6}, \quad (5)$$

shows an even stronger scaling of $C_6 \propto n^{11}$. One should note that the precise form of the interaction potentials may become increasingly complex, especially for interactions between states with non-zero orbital angular momentum.^[11–13] Accordingly, dedicated software packages for calculating Rydberg atom interaction potentials have been developed.^[14,15] Another deviation from the simple hydrogen model results arises due to the presence of additional electrons and protons in every atom of higher atomic number than hydrogen. Even for alkali atoms, where the additional electrons form closed shells, the core electrons will cause screening of the effective potential seen by the outer electron, which in turn results in deviations from the standard $\frac{1}{r}$ -behavior. These effects may be handled using quantum defect theory,^[1] which effectively corresponds to replacing the bare quantum number n with an effective quantum number $n^* = n - \delta_l$, where δ_l is the so-called quantum defect for states with angular momentum l . As electron states with low angular momentum values yield higher probabilities to find the electron in the vicinity of the core, quantum defects become smaller with increasing l and as screening always reduces the magnitude of the interaction energy, they are always positive for atoms.

While the properties and features of Rydberg atoms mentioned above are already impressive, their feasibility for applications in quantum technologies relies on a subtle effect called Rydberg blockade. When an atom is excited from the ground state toward a Rydberg state via optical excitation, the energy needed to excite a second atom in its vicinity to a Rydberg state as well will be modified by the van-der-Waals interaction energy U_{vdW} between the two atoms. If this energy separation becomes larger than the linewidth of the laser used to drive the transition, it will be impossible to promote a second atom towards a Rydberg state within a certain blockade radius around the first one. These long-range Rydberg interactions have been at the heart of many building blocks such as gates^[16] and qubits^[17] for quantum technologies based on neutral atoms.^[2]

3. Semiconductor Rydberg Systems

Generally speaking, any bound electron system may show a Rydberg series of states. Excitons as hydrogen-like complexes are prime candidates for investigations of Rydberg physics inside



Marc Aßmann received his Ph.D. degree in semiconductor spectroscopy from TU Dortmund University, Germany, in 2010. In 2013 he spent a year as a Feodor–Lynen fellow of the Humboldt foundation at JILA in Boulder, CO, USA. In 2014 he joined TU Dortmund again, first as a postdoc, then as a junior professor. His current research interests include the frontier between semiconductor physics, nanophotonics and quantum optics.



Manfred Bayer has studied physics at the University of Würzburg, Germany, finishing with a diploma thesis in theoretical elementary particle physics, before turning to laser spectroscopy of semiconductor nanostructures in his Ph.D. thesis, which he completed in 1997. After his habilitation in 2000 he was appointed as full professor at TU Dortmund in 2002.

a semiconductor environment. Still most experimental studies focus on ground state excitons and only in few material systems such as Cu_2O ^[6] or TMDs,^[18] observation of Rydberg states has been reported experimentally. To clarify the reason for this, we will first discuss the general differences between excitons in semiconductors and Rydberg atoms and the specific properties of Cu_2O , which render it an ideal material system for semiconductor Rydberg physics.

Also for excitons in semiconductors, the Rydberg energy is still given by Equation (3). However, compared to atoms there are two major differences. First, excitons reside inside a medium that screens Coulomb interactions, so its relative permittivity ϵ_r is larger than 1. Second, while for atoms the masses of electron and proton differ significantly, the effective masses of the electrons and holes that make up the excitons are of the same order of magnitude and may be significantly smaller than the free electron mass. Both effects reduce the Rydberg energy for excitons. The reduction due to the effective mass depends strongly on the band structure of the material. As holes are much lighter than protons, this effect usually amounts to a reduction by a factor of at least 2, but may become much larger for materials with low effective electron and hole masses. The contribution of the dielectric constant is proportional to the fourth power of the refractive index of the material. For Cu_2O , the material that hosts the highest observed Rydberg states inside a semiconductor system so far, the refractive index is approximately 2.7. Accordingly, compared to hydrogen, the Rydberg energy is reduced by a factor

of approximately 53. The effective electron and hole masses of $0.99 m_e$ and $0.58 m_e$ result in a reduced exciton mass of $\mu_{\text{Cu}_2\text{O}}$ of 0.366, which corresponds to another binding energy reduction by a factor of about 2.7. In total, compared to hydrogen, which features a Rydberg energy of about 13.6 eV, the exciton binding energy for Cu_2O —which is equivalent to the Rydberg energy—is on the order of 90 meV, which matches the expected reduction by a factor of approximately 145 well.

As Cu_2O is outstanding with respect to the possibility to observe the Rydberg series in semiconductors, it is worthwhile to discuss what makes the observation of Rydberg states in semiconductors much harder to achieve compared to atoms and which material properties to look for, if one tries to find other material systems that might show Rydberg exciton states. To this end, we will mention principal differences between cold atoms and excitons and compare the material properties of Cu_2O to the prototypical semiconductor system GaAs. First, one obvious difference between cold atoms and excitons is simply given by their surroundings. An atom is an individual entity that may be placed in vacuum, while the exciton will necessarily exist in a semiconductor surrounding. Accordingly, it is not possible to completely decouple excitons from their surroundings and they may interact with any kind of carrier or excitation that may be present inside the crystal. This includes defects present inside the material such as charged impurities or charges that may be present at the surface of the crystal sample as well as intrinsic excitations present inside solid-state systems such as phonons. Especially the latter may contribute to the linewidth of the exciton modes and result in much faster population dynamics compared to cold atom physics. Another quite important feature that renders excitons different from cold atoms is that they necessarily constitute open systems. While the 1S state of an atom usually is the true ground state of an atom, the electrons and holes that make up the excitons require excitation of an electron from the valence to the conduction band. Excitons are thus excited states of the system that may recombine radiatively. Accordingly, they bear some similarity with positronium and they may decay to the true ground state of the system, where the conduction band is unoccupied. The latter state is sometimes cautiously called the crystal vacuum. For some purposes, this is a clear disadvantage compared to Rydberg atoms. For example, one may confine a ground state atom in space with quite high precision and then go on to create excited Rydberg states at well defined positions quite easily, while optically created excitons are usually created at random positions within the light beam used to excite them inside the material, which makes it harder to achieve control of their positions. Along the same lines, it is in principle possible to induce transitions between different Rydberg exciton states, but the energy required to do so is usually in the Terahertz range, which is quite demanding with respect to the light sources one may use and the spot sizes one may achieve.

On the other hand, Rydberg excitons open up the possibility to investigate the properties of open systems much more easily as compared to their atomic counterparts. Along similar lines, also the typical experiments will look very different in both cases. Due to the large Rydberg energy of atoms, the individual states are usually spectrally narrow and the number of states within a typical tuning range of the lasers involved is small. Accordingly, one usually identifies one or few states of interest and studies their

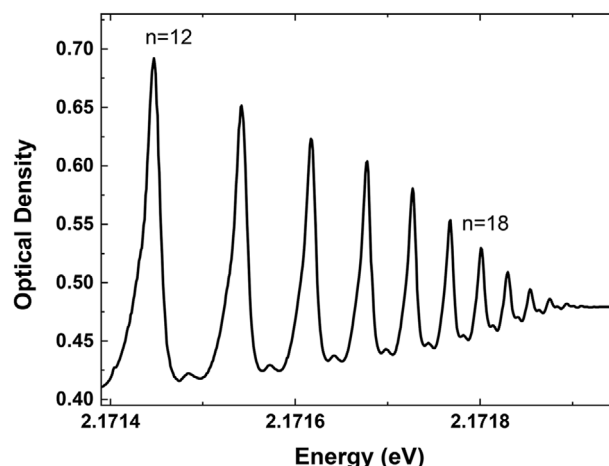


Figure 1. High-energy region of the Rydberg exciton series in Cu_2O . The region between $n = 12$ up to the band gap is shown.

properties. Excitation protocols may involve using several lasers simultaneously in order to reach some state of choice via intermediate states. In semiconductors, the Rydberg energy is much lower, so that the whole spectral range from the 1S exciton to the band gap may often be covered by a single tunable laser. This renders systematic investigations across states with several different principal quantum numbers easy. However, as the different levels are close in energy and the presence of phonons may introduce transitions between these states, it is hard to study truly isolated states and the possible relaxation towards other states and the dynamics of such processes always need to be taken into account.

Among the huge number of available semiconductor materials, Cu_2O holds a quite unique position with respect to the possibility to investigate Rydberg exciton states. A typical absorption spectrum of a thin slab of Cu_2O is shown in Figure 1.^[6] The special material properties of Cuprous Oxide make it a very suitable material for such studies. If one tries to identify different materials that are suitable for studies of highly excited exciton states, they should ideally share some of the properties of Cu_2O . In the following, we briefly discuss what renders a material suitable to host Rydberg excitons.

First, the exciton binding energy of about 90 meV in Cu_2O is much larger than the exciton binding energy of about 4.2 meV one finds in GaAs, which is often considered as the prototypical conventional semiconductor for exciton studies. Considering that the binding energy of the exciton states scales as n^{-2} , there will be a cutoff in the largest observable principal quantum number n_{max} due to thermal ionization for any finite temperature, which is given by

$$n_{\text{max}} \approx \sqrt{\frac{E_B}{k_B T}}. \quad (6)$$

Even assuming a rather low temperature of 1.35 K, this means that states above $n = 6$ will already be mostly ionized for GaAs, while n_{max} will be on the order of 28 for Cu_2O . Further, also the level spacing between adjacent levels of the same n scales with E_B . Therefore, in materials with small exciton binding energies, already moderate amounts of inhomogeneous broadening

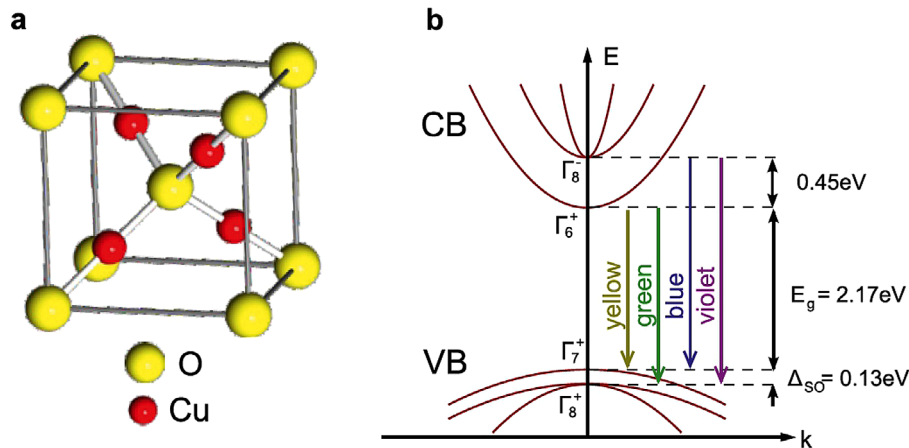


Figure 2. Crystal structure of Cu_2O . Left: Elementary cell of Cu_2O . The oxygen atoms form a bcc sublattice, while the copper atoms form a fcc sublattice. Both sublattices are shifted by a quarter of the diagonal with respect to each other. Right: Schematic electronic band structure close to the center of the Brillouin zone including the symmetries of the bands. The transitions between the two valence bands and two conduction bands result in four series of excitons, called yellow, green, blue and violet series, respectively. Adapted with permission.^[6] Copyright 2014, Springer Nature.

caused by strain, defects or other sample inhomogeneities will wash out the higher resonances. Another reason why Cu_2O is an ideal system for the observation of highly excited Rydberg states is given by its peculiar band structure, which is depicted in **Figure 2** along with the parities and symmetries of the bands. The latter are given by the irreducible representations of the relevant point symmetry group O_h for Cu_2O , which correspond to all operations that map a cube onto itself.^[19] The band structure shows several exciton series in the visible regime. However, for investigations of Rydberg states, we will focus mostly on the lowest energy series, which is the so-called yellow series.

The two highest valence bands of Γ_7^+ and Γ_8^+ symmetry originate from Cu 3d electrons and taking the crystal field and spin-orbit coupling into account, respectively, while the lowest conduction band of Γ_6^+ stems from Cu 4s electrons.^[20,21] Accordingly, Cu_2O is an example for a material, where electrons and holes do not only originate from the same ion, but the valence and conduction band states also share the same parity. Therefore, direct dipole transitions between these bands are forbidden. Transitions toward hydrogen-like exciton states, however, offer the angular momentum of the relative motion between electron and hole as an additional degree of freedom, so excitons with a P -envelope may be excited via direct dipole transitions. As P -states exist only for $n = 2$ and higher principal quantum numbers, this has the peculiar consequence that there is no dipole emission from the lowest energy exciton states with $n = 1$. This state shows quite special properties. Due to the small spatial extension of the excitons, so-called central cell corrections need to be taken into account, which results in an enhancement of its binding energy to about 150 meV and therefore deviations from the typical hydrogen-like spectrum.^[22–25] Further, the 1S state is split into a threefold degenerate orthoexciton state and a paraxciton state, where the former is shifted to higher energy by approximately 12 meV due to exchange interaction.^[26] Optical transitions from the orthoexciton are quadrupole-allowed, while optical recombination processes from the paraxciton state as spin-triplet state are forbidden up to all orders. Thus, the lowest energy exciton

state in the system is a dark state. With respect to the ability to observe highly excited states, this is an important advantage compared to many other semiconductor materials. Short-lived lowest-energy states usually show very bright and spectrally broad emission. In real experimental spectra this may result in Rydberg state absorption showing up only as small features on a huge background arising from the $n = 1$ state, while its absence makes it much easier to observe the Rydberg states in forbidden direct-gap semiconductors such as Cu_2O . Still, a different kind of background exists even for most forbidden direct-gap systems: Phonon-assisted transitions to the 1S states are still possible if phonons of matching parity exist in the system. For Cu_2O , the most relevant phonon is the optical Γ_3^- -phonon at an energy of 13.6 meV.^[27,28] Phonon-assisted transitions to the 1S excitons of the green and yellow series are possible and form a continuous background on which the series of Rydberg exciton states resides. A typical full spectrum of Rydberg resonances including the most important contributions to the phonon background is shown in **Figure 3**. As can be seen clearly, the Rydberg exciton resonances show a characteristic asymmetric line shape that corresponds to a Fano resonance. This peculiar line shape is caused by interference between absorption to the spectrally narrow exciton states and the continuous phonon background. The individual absorption lines are described well by the typical asymmetric Fano lineshape^[29]

$$\alpha_n(E) = A_n \frac{\frac{\Gamma_n}{2} + 2q_n(E - E_n)}{\left(\frac{\Gamma_n}{2}\right)^2 + (E - E_n)^2}, \quad (7)$$

where A_n denotes the resonance amplitude that is proportional to the oscillator strength, Γ_n represents the linewidth of the nP state and E_n is the resonance energy, which does not necessarily coincide with the peak of the resonance due to the asymmetry that is described by the asymmetry parameter q_n .

Further, it is worthwhile to discuss whether it is sufficient to consider bare excitons in optical experiments or whether they actually need to be treated as polaritons. For dipole transitions

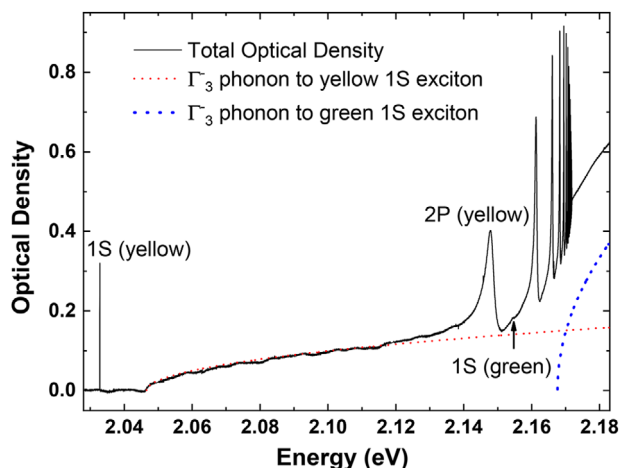


Figure 3. Full spectrum of the Rydberg exciton series in Cu_2O including the phonon background. The most important contributions to the background arise from Γ_3^- -phonon assisted transitions to the 1S excitons of the green and yellow series, respectively. The resonances acquire a typical Fano lineshape due to interference between absorption to the discrete modes and the continuum of background modes. Note on the low energy side of the spectrum the quadrupole transition to the 1S exciton with an extremely narrow linewidth in the μeV -range.

toward exciton states, contradicting theoretical predictions have been presented, ranging from exciton spectra that show clear polariton splittings for almost all principal quantum numbers^[30] to the prediction that polariton effects are negligible for principal quantum numbers below 29 and therefore polariton splittings should not be observable in experiments.^[31] So far, no experimental signatures of a polariton splitting in experimental transmission spectra on dipole transitions have been observed, which implies that for P-excitons polariton effects are relevant only for principal quantum numbers larger than those usually encountered in experiments. However, it should be noted that actually two kinds of polaritons may exist.^[32] For experiments such as transmission experiments, where polaritons with a fixed energy are created, the criterion for the occurrence of polariton effects is given by the spatial coherence of the polaritons. On the contrary, in experiments, where polaritons with a fixed wavevector are created, for example, using two-photon absorption, the criterion for the occurrence of polariton effects is given by temporal coherence of the polaritons. Temporal coherence is usually much easier to accomplish in experiments than spatial coherence. Accordingly, although polariton effects do not seem to play a prominent role in transmission experiments on P-excitons, they clearly need to be taken into account in experiments based on sum frequency generation or quadrupole transitions.^[33,34] As an example for the latter, note that for the 1S orthoexciton and the paraexciton in magnetic field polariton propagation beats were observed despite the small oscillator strength from the quadrupole transition, which was counterbalanced by their superior coherence properties.

For systems, where polariton effects become relevant, several intriguing effects based on the coherence between the light field and the excitons have been proposed including self-phase modulation^[35] and Franz–Keldysh oscillations.^[36] However, none of them have been observed in experiments so far, which again

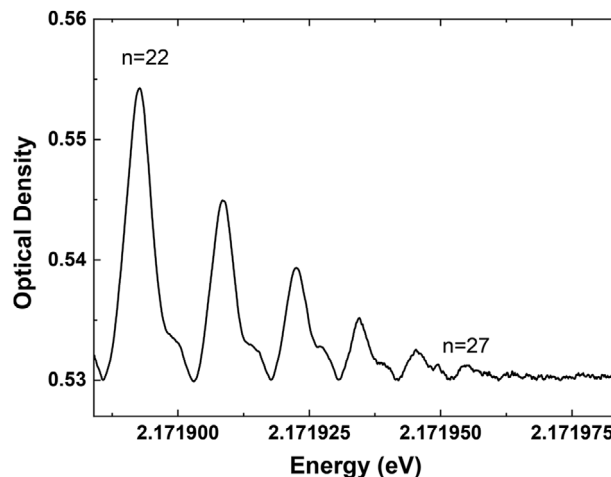


Figure 4. Rydberg exciton spectrum close to the band gap at a low temperature of about 50 mK. Note that the total spectral range shown here amounts to 100 μeV only.

implies that polariton effects are of limited importance for P-excitons in Cu_2O . Still it may be very worthwhile to look for these effects in other material systems that give rise to Rydberg excitons.

4. Rydberg Exciton Interactions

As discussed before, the presence of phonons also plays a decisive role for the highest principal quantum number one may observe in a system. It provides a temperature-dependent upper limit according to Equation (6). At 1.7 K one may expect to see Rydberg exciton states up to $n = 25$, which matches the observations in experiments using standard bath cryostats well. Experiments in dilution cryostats that are able to achieve temperatures in the millikelvin range are therefore very interesting in order to observe states of even higher principal quantum number. A typical spectrum taken at a temperature of 50 mK is shown in **Figure 4**. It is apparent that the resonances become more clearly defined and n_{max} increases to about 28 at this significantly lowered temperature.

However, considering solely the limit to n_{max} given by thermal ionization, one would expect to find resonances up to about $n = 145$ in the spectrum at this temperature. As this difference is quite large, this observation implies that other mechanisms exist, which limit the stability of high- n states so that they smear out and merge with the continuum. This result is highly interesting as due to their large spatial extent Rydberg excitons are prime candidates for semiconductor-based precision sensing. The mechanisms that reduce the absorption toward Rydberg exciton states open up the possibility to study their interaction mechanisms both with each other and other particles in detail. As it turns out, two very different interaction mechanisms arise: First, Rydberg excitons show significant interactions with free carriers present in the system. Their presence results in a band gap shift that is decisive for n_{max} , especially for non-resonant excitation of the system. Second, the interaction between different Rydberg excitons is quite large, so that the energy required

to create a second exciton in the vicinity of one that already exists becomes modified by their interaction energy. This energy shift may become larger than the linewidth of the laser used for excitation which results in vanishing absorption to the excited exciton state. This effect is termed Rydberg exciton blockade in full analogy to the similar mechanism well known from cold atoms and is most decisive for resonant excitation of the system. In the following we discuss both mechanisms in detail.

4.1. Plasma Blockade

It is well known that semiconductor systems show a smooth transition from an excitonic insulator phase toward an electron–hole plasma with increasing exciton density.^[37,38] This transition usually occurs at the Mott density, where the mean carrier separation becomes comparable to the exciton radius. The Mott transition has been studied in quite some detail for 1S excitons in several materials by means of photoluminescence experiments.^[39–42] However, these yield only limited information due to the peculiar nature of the Mott transition.

While the Mott transition may be considered as the equivalent to ionization of Rydberg atoms, one should clearly point out the differences between them. For atoms, the relevant experimental reference energy is that of the 1S state, which is located one Rydberg energy below the ionization continuum. Standard experiments investigate transitions between the ground state and some excited state. In the presence of screening, the binding energies of Rydberg states are reduced and both the ground and the excited state shift closer to the ionization continuum. The energy difference between the ground and the excited state becomes reduced as well, so effectively the excited state suffers a redshift. For excitons, however, the situation is quite different. The ground state of the system is not the 1S exciton, but the empty crystal devoid of any excitons. Here, optical excitation directly creates Rydberg exciton states, so the relevant reference energy is the valence band energy, which plays the role of the 1S state of atoms in atomic physics. Accordingly the conduction band energy is the equivalent of the onset of the ionization continuum and the band gap corresponds to the energy difference between the ground state and the continuum. The onset of the Rydberg exciton series will be located one exciton binding energy below the band gap. Therefore, the 1S exciton state is already the first excited state of the system. Accordingly, in strong contrast to the case in atomic physics for a constant band gap the reduction of the Rydberg state binding energies caused by screening would actually result in a blueshift of the energy levels of the Rydberg exciton series relative to the valence band. However, the situation is even more sophisticated. Screening also effects the energy of the electron bands and accordingly the band gap becomes reduced, which in turn results in a redshift of the Rydberg exciton states. It is a very peculiar feature of semiconductor physics that when all many-body effects that renormalize the energy levels, such as phase space occupation, exchange self-energy, dynamical self-energy correction and the screening of the effective potential are taken into account, all of these effects compensate each other such that the exciton lines initially do not shift or broaden at all.^[43,44] In fact, for most materials, energy shifts and

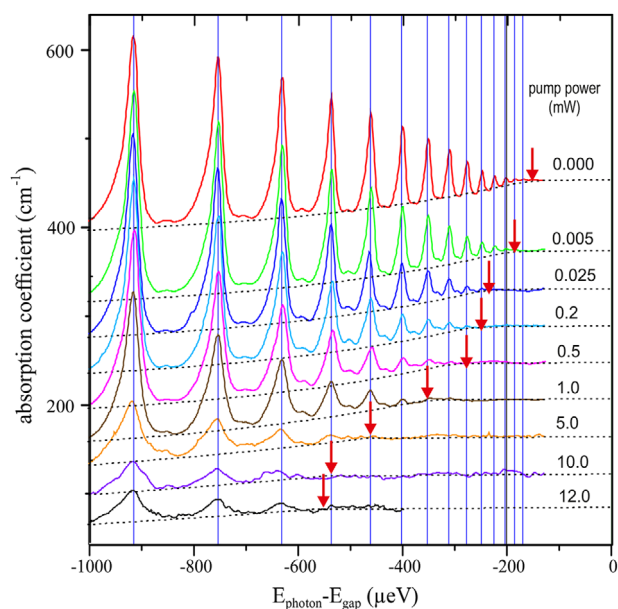


Figure 5. Absorption spectra of Rydberg excitons at 1.35 K in the presence of an additional cw pump beam at an energy of 2.2 eV. The top trace shows the bare absorption in the absence of any pump beam. Dashed lines represent the continuum absorption and the Urbach tail-like background absorption below the band gap. Arrows identify the position of the band gap. Traces are shifted vertically for clarity. The zero-energy position of the x-axis corresponds to $E_{\text{gap}} = 2.17208$ eV. Adapted with permission.^[46] Copyright 2018, American Physical Society.

spectral broadening of exciton states appear only very close to the Mott transition, where the band gap approaches the exciton line. This renders experimental investigations of band gap renormalization a highly non-trivial problem that usually requires a line shape analysis based on theoretical models. Techniques such as angle-resolved photoelectron spectroscopy that directly measure the momentum-resolved band energies are applicable, but usually yield a rather coarse resolution.^[45]

Interestingly, it is exactly this insensitivity of exciton lines to the presence of a surrounding plasma that opens up the possibility to monitor band gap renormalization using Rydberg exciton states with good spectral resolution.^[46] Just like ground state excitons, Rydberg exciton lines do not shift or broaden significantly unless the band gap energy approaches the exciton energy. At this point, the excitonic resonance begins to become smaller in magnitude and finally vanishes completely when the band gap crosses the resonance and the exciton becomes ionized. Here, its oscillator strength becomes redistributed to the continuum. Accordingly, it becomes possible to identify the band gap energy at the discrete points where it crosses exciton resonances. As the plasma density required to ionize an exciton state is known to scale as n^{-4} , this opens up the possibility to gain systematic insights into the Mott transition and band gap renormalization with high spectral resolution.

Figure 5 shows absorption spectra of a Cu_2O crystal slab with a thickness of 30 μm at a temperature of 1.35 K from $n = 10$ up to the band gap. The topmost trace shows the bare Rydberg series absorption spectrum measured using a frequency stabilized dye laser. One can clearly identify the onset of the band gap as the

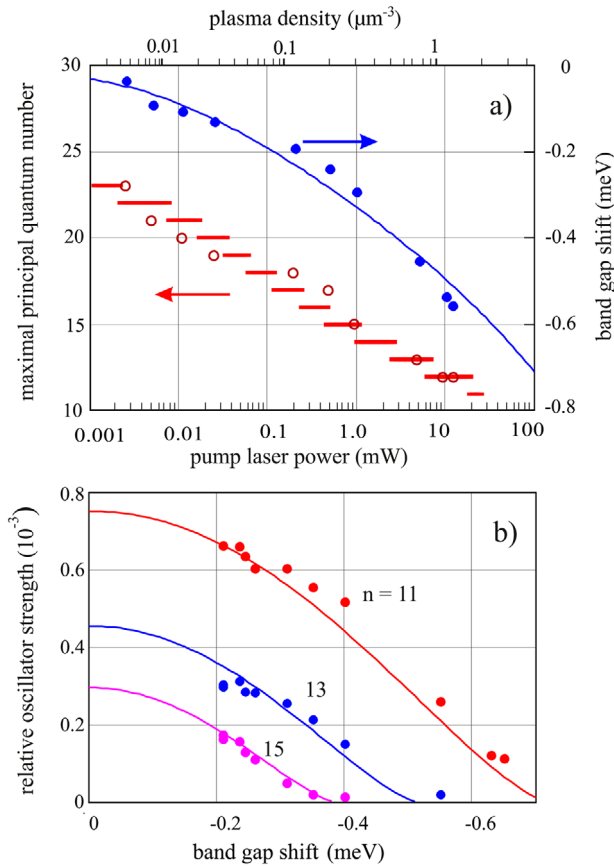


Figure 6. Upper panel: Highest observed principal quantum number (red, left abscissa) and band gap shift (blue, right abscissa) versus pump power. The experimental data follows the scaling laws of $\rho_{eh}^{-0.25}$ and $\rho_{eh}^{0.5}$, respectively expected from theory. Lower panel: Experimentally determined relative oscillator strengths (dots) of Rydberg excitons in the presence of a plasma for $n = 15, 17,$ and 19 . Lines correspond to theory results based on a modified Bohr radius determined via a variational approach. Adapted with permission.^[46] Copyright 2018, American Physical Society.

region where the spectrum begins to become approximately flat. A second frequency-stabilized dye laser set to an energy approximately 28 meV above the bandgap is used to optically inject free electrons and holes into the system. The corresponding absorption spectra are also shown in Figure 5. Here the optical power increases from top to bottom and the range of applied power densities lies between 50 and 120 mW/mm². Surprisingly, already for the lowest pump powers, the absorption of the exciton states decreases. With increasing pump power, an increasing number of exciton lines vanishes completely, starting from the states with highest principal quantum number. For the strongest pump, states above $n = 12$ are not observable in the experiment. As states disappear when the band gap crosses them, this establishes an unambiguous connection between the pump power and the corresponding band gap shift.

Figure 6 shows the key results one may gather from these spectra. The upper panel shows the band gap shift and the maximum observable principal quantum number for the different pump powers. The lower panel shows how the oscillator strengths of three selected exciton lines decrease in response to the shifting

band gap. Within experimental accuracy of about 1 μeV no notable changes of the exciton energies or linewidths occur. This immediately shows that the reduced oscillator strength of the exciton resonances is not related to scattering processes with the plasma. The reduced lifetime that accompanies such processes would result in a significant broadening of the resonances. The results rather point toward changes in the excitonic envelope functions via plasma dressing. Such effects are well known from atoms.^[47,48] Another experimental observation indicating strongly that incoherent scattering between the excitons and the plasma is not a significant effect is the continued presence of the intermediate peaks between two Rydberg exciton resonances even in the presence of a plasma. These resonances correspond to a coherently driven V-type system consisting of two Rydberg exciton states connected to the same ground state.^[49] Any dephasing introduced by incoherent scattering between excitons and free carriers would prevent excitation of these coherent superposition states. Instead these intermediate resonances continue to exist until the band gap reaches the higher-energy resonance, which shows that initially there is no dephasing due to incoherent scattering with the plasma.

For Cu_2O the plasma density at which the Mott transition occurs for the 1S exciton is well known and amounts to $3 \times 10^{18} \text{ cm}^{-3}$. Obviously, the similar vanishing of Rydberg resonances takes place at much lower plasma densities. Relating the pump powers observed in the experiment to plasma densities ρ_{eh} inside the sample directly is a non-trivial task, but it is possible to give at least some estimates.^[46] For the experimental results shown here, the plasma density is quite small. One may treat the electron–hole plasma within the framework of classical non-degenerate Debye theory. Here, the correlation part of the chemical potential Δ_D approximates the band gap shift Δ well. Its dependence on plasma density and temperature will therefore allow one to establish a connection between the plasma density and the number of resonances observable in experimental spectra. Δ_D is given by

$$\Delta_D = -\frac{\kappa e^2}{4\pi\epsilon_0\epsilon_b}, \quad (8)$$

where κ represents the inverse screening length. An electron–hole-plasma is a two-component plasma, where the electron and hole subsystems may have different temperatures, T_e and T_h , which in turn may both be different from the lattice temperature. Considering an effective screening temperature $T_{sc}^{-1} = (T_e^{-1} + T_h^{-1})/2$, the inverse screening length for a two-component plasma is given by

$$\kappa^2 = \frac{2\rho_{eh}e^2}{\epsilon_0\epsilon_b k_B T_{sc}}. \quad (9)$$

Accordingly, for constant temperature $-\Delta_D$ is expected to scale as $\sqrt{\rho_{eh}}$. One may assume that an exciton line should vanish into the continuum when the chemical potential shifts the band gap below the energy resonance. As the binding energy of the Rydberg states scales as n^{-2} , one expects the critical plasma density $\rho_{eh,c}(n)$ at which the exciton states merge into the continuum to scale as n^{-4} . One may then convert the experimentally applied pump powers to the plasma densities used in theory via

a set of rate equations. As a result, the scaling law predictions agree well with experimental data as shown in the upper panel of Figure 6. As a second experimental signature one may also compare the oscillator strength $f_{\text{osc}}(n)$ of the different Rydberg exciton states in the presence of a plasma to the experimentally determined values shown in the lower panel of Figure 6. For P -excitons, the oscillator strength depends mostly on the slope of the exciton envelope wave function at vanishing separation between electron and hole:

$$f_{\text{osc}}(n) \propto \left(\frac{\partial \phi(r)}{\partial r} \Big|_{r=0} \right)^2 = \frac{n^2 - 1}{3\pi a_B^5 n^5}, \quad (10)$$

which in turn depends only on the principal quantum number and the exciton Bohr radius a_B . In the low plasma density limit considered here, it is sufficient to consider that the hydrogen-like exciton wave function gets modified in the plasma-screened Coulomb potential. Using a variational approach, one finds that the effective exciton Bohr radius $a_{B,\text{eff}}$ in the screened potential becomes larger compared to the bare exciton Bohr radius. In order to incorporate the effect that the resonances do not show observable shifts, one may assign new effective quantum numbers n_{eff} to the resonances, such that their energies remain unchanged. The values of both $a_{B,\text{eff}}$ and n_{eff} are shown in the lower panel of Figure 7. $a_{B,\text{eff}}$ increases already for low plasma densities, reflecting the spatial exciton extension becoming larger in the screened potential. In contrast, n_{eff} shows only small changes at low plasma densities, but diverges close to the point of ionization, where the band gap reaches a resonance. Assuming that the screening leaves the symmetry of the exciton states mostly intact, so that Equation (10) is still valid, it is this divergence of n_{eff} that contributes strongly to the reduced oscillator strength of the exciton resonances. The lower panel of Figure 6 shows the expected oscillator strength dependence on the band gap shift for several principal quantum numbers. The results are clearly in good agreement with experiment.

Besides that, the theory allows one to gain some deeper insights into the material system at hand. First, as shown in the upper panel of Figure 7, at 1.35 K, for the $n = 25$ state $\rho_{\text{eh},c}(25) \approx 10^{-2} \mu\text{m}^{-3}$, which is eight orders of magnitude below the comparable 1S exciton Mott density. This density corresponds to a screening length of about 1.6 μm and a total band gap renormalization of about 150 μeV . Still, this small band gap shift and the plasma densities required to achieve it may be resolved well in experiments by finding the energies, where the absorption spectrum transforms from the Rydberg exciton series located on a smoothly increasing background into a flat absorption spectrum without pronounced resonances for each pump power. Therefore, Rydberg states open up the possibility to investigate even tiny band gap shifts with excellent spectral resolution.^[50] Second, in order to achieve reasonable agreement with the experiment, one has to distinguish between the band gap shift caused by non-resonant pumping and the intrinsic band gap shift that arises due to the presence of charged impurities. The latter may be considered as an offset that is always present and corresponds to an uncompensated carrier density of $0.01 \mu\text{m}^{-3}$. Although this is not a huge number and may vary slightly across different samples and even different sample positions, it turns out that this small contribution results in band gap shifts on the order of 100–

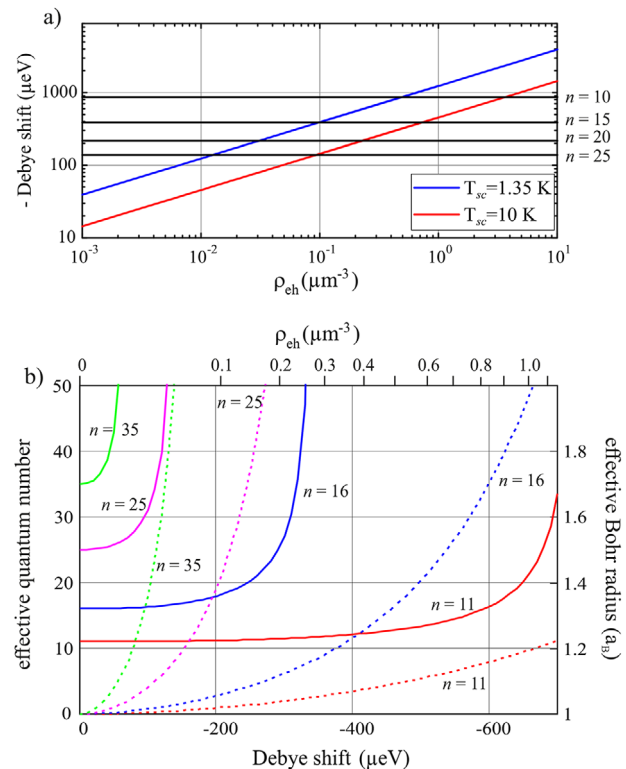


Figure 7. Upper panel: Correlation part of the chemical potential versus plasma density for $T_{\text{sc}} = 1.35 \text{ K}$ and $T_{\text{sc}} = 10 \text{ K}$. Horizontal lines correspond to binding energies of selected Rydberg exciton states. Line crossings correspond to the critical plasma densities required to ionize the states. Lower panel: Effective principal quantum number n_{eff} (full lines) and effective exciton Bohr radius $a_{B,\text{eff}}$ (dashed lines) versus the correlation part of the chemical potential for several n . The upper abscissa shows the corresponding plasma density for a plasma temperature of 5 K. Adapted with permission.^[46] Copyright 2018, American Physical Society.

150 μeV that are sufficient to ionize resonances above $n = 25$ to $n = 28$. Accordingly, it is indeed the density of impurities present within the sample that gives the upper limit for the observable Rydberg states in Cu_2O . Another question is whether a mean-field approach such as applying Debye theory is the correct description for an extremely dilute plasma at densities at which one nevertheless already observes changes of the band gap energy. If the zero density shift is indeed caused by charged impurities, an alternate description might be that the electric fields by these charges lead to a tilting of the Coulomb potential between electron and hole by which the highly excited states above $n = 25$ can dissociate through tunneling and they become in effect located in a continuum.^[51,52]

4.2. Rydberg Blockade

Besides the interaction between Rydberg excitons and free carriers, also the interaction between different excitons is highly interesting as the large spatial extension of Rydberg exciton states also enhances the exciton–exciton interaction significantly. For 1S excitons, exciton–exciton interactions are usually rather small and may be described in terms of zero-range collisions.^[53] In

this case, exchange interaction terms become dominant and the direct Coulomb interaction becomes negligible. For highly excited states the relative importance of these contributions may become reversed.^[54] From a fundamental aspect, this is very interesting as exciton interactions become long-ranged and depend on the relative distance between two excitons. Probably the most interesting effect resulting from such long-range interactions^[11] is the so-called Rydberg blockade.^[2] In the presence of an exciton, the energy required to excite a second exciton directly next to it will be modified by the interaction energy between these two excitons. Due to the long-ranged nature of the interactions, this energy shift will acquire a spatial dependence. Accordingly, whether a second exciton may be excited in the vicinity of the first one becomes a question of the spectral width of the light field used to create them. If at some position the spectral shift due to interactions becomes so large that there is no overlap with the spectrum of the light source, excitation of a second exciton becomes impossible. This effect is the Rydberg exciton blockade. In the limit of a light source that is spectrally narrow compared to the linewidth of the Rydberg exciton states, the blockade condition becomes simplified. Assuming isotropic interactions, one may define an exciton blockade radius $R_C(n)$ around an exciton, inside which the interaction energy becomes larger than the linewidth Γ_n of the respective states and no further excitons of the same quantum number can be created. The corresponding blockade volume is given by $V_B = \frac{4}{3}\pi R_C(n)^3$.

Identifying Rydberg exciton blockade in experimental spectra is a highly non-trivial task. A prominent experimental signature of non-linear interaction-induced effects is the redistribution of oscillator strength from the resonances towards other parts of the spectrum for different optical excitation powers P_L , which manifests in the power-dependent absorption signal $\alpha(E, P_L)$. For absorption directly at the resonances, the absorption $\alpha_0(E) = \alpha(E, 0)$ of the unexcited crystal should show the highest obtainable absorption. Each exciton present within the crystal will now reduce the space, where further excitons may be excited by one blockade volume. Accordingly, for an exciton density ρ_X , the absorption is supposed to scale as $\alpha(E, P_L) = \alpha_0(E) - \rho_X V_B$. The exciton density itself is given by the product of the absorption $\alpha(E, P_L)$, the laser power P_L and the exciton lifetime τ_n , which scales as the inverse linewidth, so $\rho_X \propto \frac{\alpha(E, P_L) P_L}{\Gamma_n}$. Introducing the blockade efficiency $S_n \propto \frac{\alpha_0 V_B}{\Gamma_n}$, which quantifies how efficiently the presence of excitons prevents excitation of further excitons, results in the following simple form for the power-dependent absorption:

$$\alpha(E, P_L) = \frac{\alpha_0(E)}{1 + S_n P_L}. \quad (11)$$

The scaling of S_n with the principal quantum number provides a clear signature that may be tested in experiments. It is worthwhile to discuss the scaling laws of the three terms that make up S_n individually. The linewidth Γ_n is expected to scale as n^{-3} for $n \gg 1$. As can be seen from Equation (7), α_0 scales as the ratio of the oscillator strength to the linewidth. As both are expected to scale as n^{-3} , α_0 is approximately expected to show no scaling with n . The most relevant term is the scaling of the blockade volume V_B with n as it depends directly on the nature of the exciton-

exciton interaction. As a reasonable approximation, the scaling laws for non-resonant or resonant dipole interactions between atoms introduced in Equations (4) and (5) apply to excitons as well. For large exciton separations, non-resonant dipole-dipole interactions between excitons will be most prominent. While exact diagonalization of the dipole-dipole interaction potential V_{dd} yields the strength of the interaction,^[54] perturbation theory may be applied to derive the scaling of the interaction in a more approachable manner. Using non-degenerate second-order perturbation theory, the contribution of non-resonant dipole-dipole interactions is proportional to $\frac{|(V_{dd})|^2}{\Delta_d}$, where Δ_d gives the energy difference between adjacent dipole-allowed states. It scales as n^{-3} . The interaction potential itself is proportional to the product of the dipole moments of the excitons involved, which scale as n^2 each, and falls off with the third power of the distance between them: $V_{dd} \propto \frac{p_1 p_2}{R^3}$. Accordingly, one arrives at the following scaling for the van-der-Waals-type non-resonant dipole-dipole interaction:

$$E_{vdw}(n) \propto \frac{|V_{dd}|^2}{\Delta_d} \propto \frac{\left(\frac{n^4}{R^3}\right)^2}{n^{-3}} \propto \frac{C_6}{R^6} \propto \frac{n^{11}}{R^6}. \quad (12)$$

For smaller exciton distances, the dipole-dipole interaction may become comparable to the energy separation between different exciton levels. In this case, a Förster-type resonant dipole-dipole interaction might become important. This kind of interaction will result in contributions to the interaction energy that scale as $\langle V_{dd} \rangle$. Accordingly, one expects these contributions to scale as:

$$E_F(n) \propto V_{dd} \propto \frac{C_3}{R^3} \propto \frac{n^4}{R^3}. \quad (13)$$

For any interaction that may be brought into such a power law form of arbitrary power k , the blockade radius, where the interaction energy exceeds the linewidth of the resonance, is then given by

$$R_C = \left(\frac{C_k}{\Gamma_n}\right)^{\frac{1}{k}}. \quad (14)$$

Interestingly, it scales as $n^{\frac{7}{3}}$ for both van-der-Waals and Förster-type interactions. As a consequence, V_B will scale as n^7 for both dipole-dipole interactions, which results in a characteristic scaling $\propto n^{10}$ of the degenerate blockade efficiency S_n , where a single laser is used which acts simultaneously as the pump and the probe beam. One may now compare this scaling law to the changes of the experimental spectra observed for varying pump powers. Typical power-dependent absorption spectra measured using a narrow single-mode dye laser are shown in **Figure 8**. Clearly, the high- n resonances quench completely at large pump powers, while for intermediate n the oscillator strength is reduced, but does not vanish completely.

The integrated peak areas of the individual resonances are proportional to the corresponding oscillator strengths and may be fitted to Equation (11) to determine the blockade efficiency S_n . A set of such fits is shown in **Figure 9**.

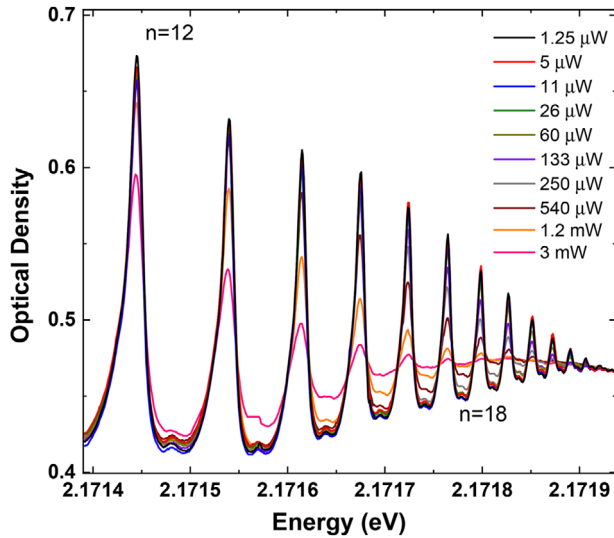


Figure 8. Transmission through a Cu_2O sample with a thickness of $34 \mu\text{m}$ at varying pump powers. As Rydberg blockade sets in, the oscillator strength of the resonances becomes reduced. States of large n are effected stronger and already at lower pump powers.

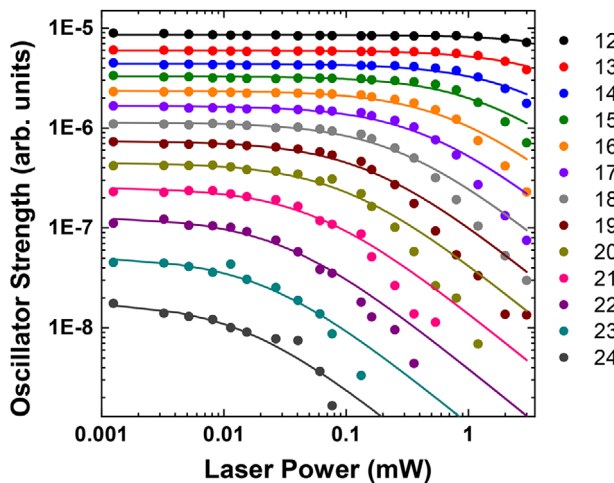


Figure 9. Oscillator strength of the individual Rydberg exciton resonances for varying laser pump powers. The onset of degenerate blockade may be identified by the reduction in oscillator strength and occurs at different pump powers for different resonances. Solid lines fit Equation (11) and give a rough estimate of the blockade efficiency. Note that Equation (11) is only expected to be valid close to the onset of blockade up to a reduction in oscillator strength of at most one order of magnitude. For higher pump powers, non-linear effects and additional effects due to the presence of other excitons and free electrons and holes become non-negligible. Adapted with permission.^[6] Copyright 2014, Springer Nature.

However, it should be noted that Equation (11) takes only blockade effects into account. As Rydberg excitons reside inside a semiconductor system, several additional effects such as interactions with other excitons, free carriers and phonons, non-linear effects, or formation of correlated exciton complexes may arise. Accordingly, the fit is expected to describe only the onset of the reduction of oscillator strength up to a reduction of about one order of magnitude at most. The blockade efficiencies for the individ-

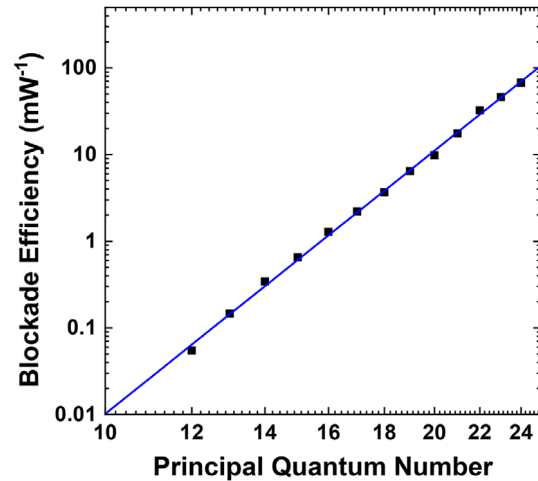


Figure 10. Blockade efficiencies determined from the fits shown in Figure 9. The solid line is a power law fit to the data, which yields an exponent of 10.09 ± 0.93 in reasonable agreement with the expected n^{10} scaling law. Adapted with permission.^[6] Copyright 2014, Springer Nature.

ual principal quantum numbers as estimated from these fits are shown in Figure 10 on a double-logarithmic scale.

The solid line corresponds to a power law fit that gives an exponent of about 10.09 ± 0.93 in accordance with what is expected in the presence of Rydberg exciton blockade. This result hints at the fact that in contrast to ground state excitons, dipole-type interactions are important when considering highly excited Rydberg excitons. However, the scaling law does not reveal whether resonant or non-resonant interactions are dominant. In order to investigate this question in detail, one has to perform non-degenerate blockade experiments, which investigate the interactions between Rydberg exciton states with different principal quantum numbers. In that case one expects different scaling laws for the blockade of states with n larger or smaller compared to the pumped Rydberg exciton state. The scaling laws and line shapes in such experiments carry more detailed information about the underlying interactions. The details go beyond the scope of this review, but the main result of such experiments is that non-resonant van-der-Waals-type interactions yield the dominant contribution to interactions between Rydberg excitons.

Therefore, it makes sense to investigate these interactions on a more detailed level. One may consider a pair of excitons i and j , where each is located at a center-of-mass position \vec{R}_i and \vec{R}_j , respectively and the relative positions of the electrons and holes making up the excitons are given by \vec{r}_i and \vec{r}_j . The individual exciton states may be described by the standard quantum numbers n , l , and m , so their states are given by $|n_i, l_i, m_i\rangle$ and $|n_j, l_j, m_j\rangle$, respectively. A schematic representation of the geometry used to describe the systems is shown in Figure 11. In general, the total interaction potential is given by the sum of the mutual Coulomb interactions between all electrons and holes that make up the excitons:

$$V^{(ij)} = \frac{e^2}{4\pi\epsilon_0\epsilon_r} \left(\frac{1}{|r_e^{(i)} - r_e^{(j)}|} + \frac{1}{|r_h^{(i)} - r_h^{(j)}|} + \frac{1}{|r_e^{(i)} - r_h^{(j)}|} + \frac{1}{|r_h^{(i)} - r_e^{(j)}|} \right). \quad (15)$$

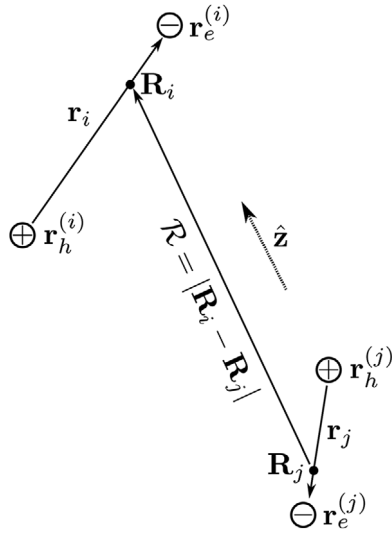


Figure 11. Sketch of an exciton pair. The individual excitons are labeled i and j and consist of electrons at positions $r_e^{(i)}$ and $r_e^{(j)}$ and holes at the positions $r_h^{(i)}$ and $r_h^{(j)}$. The center-of-mass positions of the excitons are denoted by \vec{R}_i and \vec{R}_j . The z -axis of the system, which is also the quantization axis is chosen to coincide with the distance vector $\vec{R}_i - \vec{R}_j$ between the two excitons. Adapted with permission.^[54] Copyright 2018, American Physical Society.

While for small exciton separation, the direct Coulomb interaction becomes small compared to the contributions by exchange interaction, here we are interested in the regime, where the exciton distance $R_{ij} = |\vec{R}_i - \vec{R}_j|$ is so large that exchange interactions and charge overlap interactions may be safely neglected. This is the case, if R_{ij} exceeds the Le Roy radius R_{LR} ^[11]:

$$R_{LR} = 2 \left(\langle n_i, l_i, m_i | r^2 | n_i, m_i, l_i \rangle^{\frac{1}{2}} + \langle n_j, l_j, m_j | r^2 | n_j, m_j, l_j \rangle^{\frac{1}{2}} \right). \quad (16)$$

Then the interaction may be rewritten in terms of a series of inverse powers of R_{ij} :

$$V^{ij} = \sum_{n=1}^{\infty} \frac{C_n}{R^n} = \sum_{l,L=1}^{\infty} \frac{U_{lL}(\vec{r}_i, \vec{r}_j)}{R_{ij}^{l+L+1}}. \quad (17)$$

Here, U_{lL} is given by

$$U_{lL}(\vec{r}_i, \vec{r}_j) = \frac{(-1)^L 4\pi}{\sqrt{(2l+1)(2L+1)}} r_i^l r_j^L \times \sum_m \sqrt{\binom{l+L}{l+m} \binom{l+L}{L+m}} Y_{lm}(\hat{r}_i) Y_{lm}(\hat{r}_j), \quad (18)$$

where Y_{lm} are spherical harmonics defined with respect to the axis that connects the centers of mass of the two excitons.

At large distances, the dipole-dipole term corresponding to $l = L = 1$ usually results in the dominant contribution and is approximately given by:

$$V^{(i,j)} \approx \frac{e^2}{4\pi\epsilon_0\epsilon_r} \left(\frac{r_i r_j}{R_{ij}^3} - \frac{3(\vec{r}_i \vec{R}_{ij})(\vec{r}_j \vec{R}_{ij})}{R_{ij}^5} \right). \quad (19)$$

One may now expand the interaction Hamiltonian in an exciton pair product base $|s_i, s_j\rangle = |n_i, l_i, m_i; n_j, l_j, m_j\rangle$ composed of the single-exciton states. This Hamiltonian consists of the sums of the single exciton energies as the diagonal terms and the off-diagonal coupling terms $\langle s_i, s_j | V^{(ij)} | s'_i s'_j \rangle$. One may then diagonalize the resulting interaction Hamiltonian for any given exciton distance R_{ij} . Within this approach the quantization axis may be chosen to be aligned with \vec{R}_{ij} . If one neglects the influences of the reduced crystal symmetry,^[55] this choice results in the total angular momentum $M = m_i + m_j$ being a good quantum number for the exciton pair states. Thus, one gets a series of potential curves for the different values of $|M|$.

Considering for simplicity only interactions between particles in the same single-exciton states of fixed l , one finds that there will be in total $2l + 1$ different possible values $|M|$ for the exciton pair state and each of these $(l, |M|)$ -manifolds will contain $2l + 1 - |M|$ states. This full treatment may be simplified further if the magnitude of interactions becomes small compared to the energy difference of the relevant energy levels:

$$|\langle s_i, s_j | V^{(ij)} | s'_i s'_j \rangle| \ll |E_i + E_j - E'_i - E'_j| \quad (20)$$

In this case, there will be no resonant coupling to other exciton pair states that scales as R_{ij}^{-3} and only non-resonant coupling becomes important. It can be treated in terms of degenerate second-order perturbation theory using an effective Hamiltonian:

$$H_{\text{vdw}} = \left(\frac{e^2}{4\pi\epsilon_0\epsilon_r R_{ij}^3} \right)^2 \sum_{|\alpha\rangle \notin \mathcal{M}} \frac{V^{(ij)} |\alpha\rangle \langle \alpha| V^{(ij)}}{\delta_\alpha} = \sum_{\mu} \frac{C_6^{\mu}}{R_{ij}^6} |\mu\rangle \langle \mu|. \quad (21)$$

This operator acts only within the degenerate subspaces $\mathcal{M} = \{|s_i s_j\rangle\}$ of initial two-exciton states of fixed l and M at energy $E_{\mathcal{M}}$, while the sum runs over the intermediate two-exciton energy levels $|\alpha\rangle$. δ_α is the Förster defect, which is the energy difference between the exciton pair state α and the individual exciton states: $\delta_\alpha = 2E_{\mathcal{M}} - E_\alpha$. Note that the two-exciton eigenstates $|\mu\rangle$ do not depend on the distance R_{ij} anymore and may be composed out of several pair states $|s_i, s_j\rangle$. One may now diagonalize Equation (21) in each subspace $(l, |M|)$ and finds that the C_6 -coefficients depend on the angular quantum numbers, but all of them show a general scaling law with n that may be described well by the following relation:

$$C_6(n) = n^{11} (c_0 + c_1 n + c_2 n^2). \quad (22)$$

Here, each set of angular quantum numbers will correspond to an individual set of coefficients c_0 , c_1 and c_2 as given in **Table 1**.

Table 1. nP - nP asymptotes sorted by the quantum number M and their corresponding approximate asymptotic wave functions obtained by fits in the range from $n = 12$ to $n = 25$. The van-der-Waals coefficients are given by $C_6(n) = n^{11}(c_0 + c_1n + c_2n^2)$. Adapted with permission.^[54] Copyright 2018, American Physical Society.

$ M $	composition of nP - nP asymptote $ \mu\rangle$	c_0 [aeV μm^6]	c_1 [aeV μm^6]	c_2 [aeV μm^6]
2	$\left \begin{smallmatrix} n11 \\ n11 \end{smallmatrix} \right\rangle$	3.266	0.946	-0.17
1	$\frac{1}{\sqrt{2}} \left(\left \begin{smallmatrix} n10 \\ n11 \end{smallmatrix} \right\rangle - \left \begin{smallmatrix} n11 \\ n10 \end{smallmatrix} \right\rangle \right)$	15.209	2.175	-0.039
1	$\frac{1}{\sqrt{2}} \left(\left \begin{smallmatrix} n10 \\ n11 \end{smallmatrix} \right\rangle + \left \begin{smallmatrix} n11 \\ n10 \end{smallmatrix} \right\rangle \right)$	-9.287	0.177	-0.004
0	$-0.252 \left(\left \begin{smallmatrix} n1-1 \\ n11 \end{smallmatrix} \right\rangle + \left \begin{smallmatrix} n11 \\ n1-1 \end{smallmatrix} \right\rangle \right) + 0.934 \left \begin{smallmatrix} n10 \\ n10 \end{smallmatrix} \right\rangle$	21.209	3.001	-0.054
0	$\frac{1}{\sqrt{2}} \left(\left \begin{smallmatrix} n1-1 \\ n11 \end{smallmatrix} \right\rangle - \left \begin{smallmatrix} n11 \\ n1-1 \end{smallmatrix} \right\rangle \right)$	-8.980	-0.053	0.0002
0	$0.661 \left(\left \begin{smallmatrix} n1-1 \\ n11 \end{smallmatrix} \right\rangle + \left \begin{smallmatrix} n11 \\ n1-1 \end{smallmatrix} \right\rangle \right) + 0.356 \left \begin{smallmatrix} n10 \\ n10 \end{smallmatrix} \right\rangle$	-11.358	0.158	-0.004

The interaction coefficients seem to be quite small and are mostly in the aeV to zeV range. However, the strong n^{11} -scaling of the C_6 -coefficients explains that the van-der-Waals interaction is simultaneously very important for Rydberg exciton interactions and negligible for the ground state interactions typically encountered in most materials. For the experimentally most relevant nP - nP asymptotes, six different interaction potentials U arise for the different values of $|M|$. They are shown for selected principal quantum numbers in Figure 12.

Their shape provides some additional insights into Rydberg exciton absorption spectra in the blockade regime. First, not all of the interaction potentials are repulsive, but some of them may be attractive as well. This explains some of the features seen in differential transmission spectra for non-degenerate blockade experiments. In contrast to the degenerate blockade experiments investigated before, such experiments introduce two different lasers in order to separate the pump and probe processes. The strong pump laser is spectrally tuned to some state of interest, while the weak probe laser is scanned across the whole absorption spectrum in order to monitor the transmission of the crystal. If the pump laser is modulated at a certain frequency, the transmitted pump beam will show a frequency component that is directly proportional to the difference of the probe transmission signal in the presence and in the absence of the pump beam. One may single out this frequency component using lock-in detection. The resulting signal is then directly proportional to the changes introduced by the pump beam and a sensitive probe for pump-induced blockade effects. One example for such a differential transmission spectrum is shown in Figure 13.

In this figure, positive signals correspond to a pump-induced increase of the probe beam transmission, which is the expected effect when blockade is present. Negative signals correspond to a pump-induced reduction of the probe beam transmission which is usually caused by enhanced absorption. Increased scattering of the pump beam would also result in negative signals. The signal shows several interesting features.

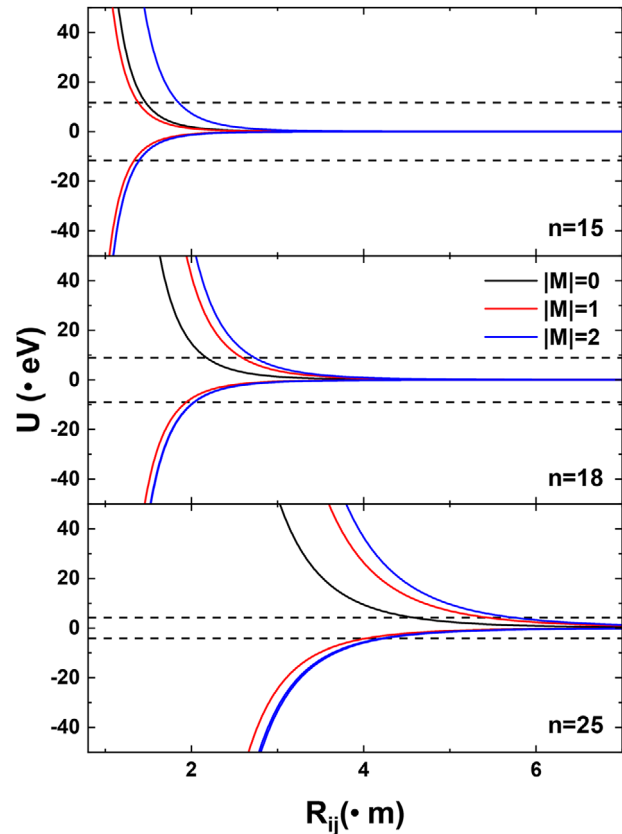


Figure 12. Asymptotic nP - nP Van der Waals interaction potentials for exciton pair states for selected n and different total angular momentum quantum numbers $|M|$.^[54] Dashed lines indicate the interaction strengths required to exceed the line widths of the corresponding nP -states. Adapted with permission.^[54] Copyright 2018, American Physical Society.

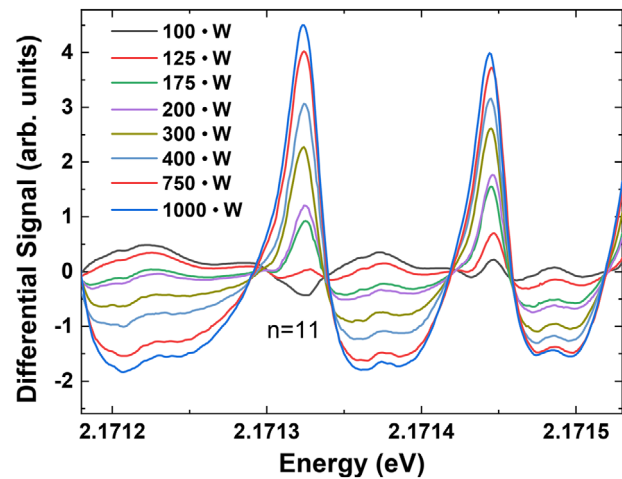


Figure 13. Differential probe transmission signal for different pump beam powers. The signal corresponds to the difference between the transmission signals in the presence and in the absence of the pump beam and directly represents the pump-induced changes. Positive signals correspond to increased transmission and correspond to blockade. Negative signals correspond to enhanced absorption.

First, the large positive signals at the peak positions that arise for large pump powers again demonstrate that the presence of the pump beam reduces the oscillator strength at the resonance peak positions and blockade is taking place. However, the signal also shows that simultaneously the probe beam absorption at energies away from the resonance energies becomes enhanced. This is not surprising per se as the total oscillator strength of the system should be conserved. However, it is remarkable that the differential signal away from the resonances is rather broad and does not show narrow spectral features and that there is a redistribution of oscillator strength both to the high and low energy sides of the Rydberg exciton peaks. Both results agree well with what is expected if exciton blockade takes place in the system. As discussed before, there are both attractive and repulsive van-der-Waals interaction potentials, depending on the value of $|M|$ of the exciton pair. Accordingly, it is expected that exciton pairs of different compositions may be excited on the high and low energy side of the resonances, respectively.

Next, the van-der-Waals interaction depends strongly on the distance between excitons. Here, a fundamental difference to cold atoms arises. In contrast to atoms, where in blockade experiments all atoms already preexist typically at well defined positions, in non-degenerate exciton blockade experiments the probe beam will create the second exciton at some distance from a pre-existing exciton created by the pump beam. Accordingly, there is no fixed energy shift for the second exciton to be created, but for any probe beam energy within the range of the van-der-Waals interaction potential around the resonance energy, there will be a preferred distance from the initial exciton, where the second exciton may be created. This results in a quite broad and featureless spectral distribution of the enhanced absorption towards exciton pair states. Strictly speaking, the excitons we consider are delocalized over the whole bulk crystal. Accordingly, it would also be more appropriate to consider the exciton pair as a delocalized state of two excitons with well-defined spatial correlations. Interestingly, this opens up the possibility to control the spatial correlations between excitons by choosing the energy of the second beam appropriately. Therefore, the Rydberg blockade observed for excitons indeed is drastically different from the one observed for atoms and therefore suited for complementary experiments compared to cold atom physics.

Further, for low pump powers one may first observe an increase of the pump-beam absorption at the exciton peak positions before the onset of blockade. This effect may be explained in relation to the plasma blockade discussed before. The presence of a small number of localized charged impurities within the crystal already results in a small shift of the band gap and a slight reduction of the oscillator strength of the resonances. An exciton in close spatial vicinity to such an impurity may become ionized and the resulting free carriers may screen the impurity or one of the resulting free carriers may be captured and neutralize the impurity, while the other free carrier may move away, for example, to the surface of the sample. In both cases, the effective influence of the impurities will become reduced, which reduces the band gap shift and increases the oscillator strength of the Rydberg exciton states within a narrow window of pump powers. This result already shows that it will not always be possible to fully isolate the appearance of Rydberg blockade and plasma blockade. Of course, free electrons and holes will form excitons

on fast timescales,^[56] while simultaneously exciton relaxation and subsequent Auger recombination^[57,58] provides a relaxation channel for excitons that may create free electrons and holes in the process. While for low-lying exciton states far away from the band gap the influence of a background of free carriers is negligible and a lot of insights into the system dynamics may already be gained by photoluminescence measurements,^[59–61] it may sometimes be difficult to fully distinguish both effects for Rydberg exciton states of very large n close to the band gap. In this case, time-resolved blockade measurements are required to fully understand the complex interplay between the different states of the Rydberg system.

5. Scaling Laws

One of the most interesting aspects of working with Rydberg states in general and Rydberg excitons in particular is the existence of characteristic scaling laws of the most important physical properties of Rydberg states. Quantities such as the exciton size or their linewidth show a characteristic power law scaling with the principal quantum number n , so they may vary over several orders of magnitude. This provides experimentalists with the opportunity to choose a set of states to work with, which matches the requirements of their experiments. This section will present a brief overview of the most relevant scaling laws for Rydberg excitons. Many of them are equivalent to the scaling laws known from cold atoms, while others differ due to semiconductor-specific effects.^[62]

Probably the most fundamental scaling law concerns the radius r_n of excitons, which depends both on n and l :

$$\langle r_n \rangle = \frac{1}{2} a_B (3n^2 - l(l+1)). \quad (23)$$

For P -excitons, the Bohr radius is $a_B = 1.11 \text{ nm}$,^[23] which results in a radius of $\langle r_{28} \rangle \approx 1.3 \mu\text{m}$ for the largest Rydberg exciton state observed so far in the absence of external fields at low temperatures. It should be noted that the yellow $1S$ -exciton does not follow this scaling law due to semiconductor-specific central-cell corrections.^[63,64] Direct measurements of the exciton radius are non-trivial, but experiments in magnetic fields hint at exciton radii that match the predicted values well for large n .^[65]

Next, the exciton binding energy is expected to scale with the inverse square of n . The experimentally determined binding energies for Rydberg exciton states up to $n = 25$ are shown in **Figure 14**. Clearly, the observed binding energies match the expected n^{-2} -dependence very well, as on this energy scale the effect of the quantum defects (relevant mostly for small principal quantum numbers) can not be resolved. Again, it should be noted that the yellow $1S$ -state does not follow this scaling law, but shows a significantly enhanced binding energy on the order of 153 meV. This is also a consequence of central-cell corrections and may be explained in an instructive manner by considering the reduced Bohr radius of this state. As this state is localized more strongly in real space corresponding to states of higher n , it is accordingly spread out more strongly in momentum space. Accordingly, the parabolic approximation for the involved bands breaks down and the non-parabolicity of the bands at higher momenta needs to

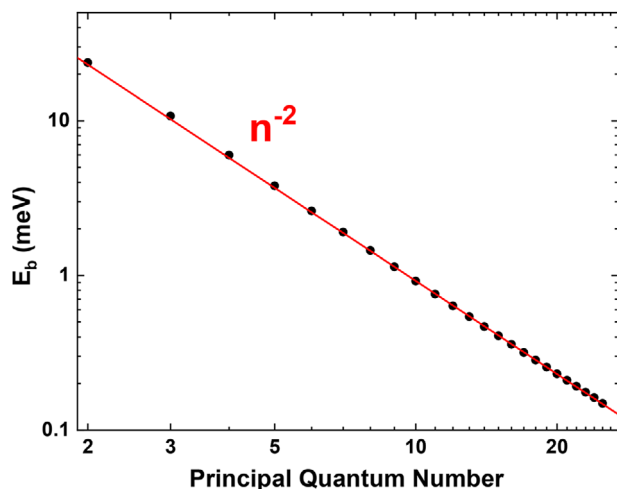


Figure 14. Rydberg exciton binding energies for different n . The binding energy shows the typical n^{-2} -scaling known from the hydrogen problem. Adapted with permission.^[6] Copyright 2014, Springer Nature.

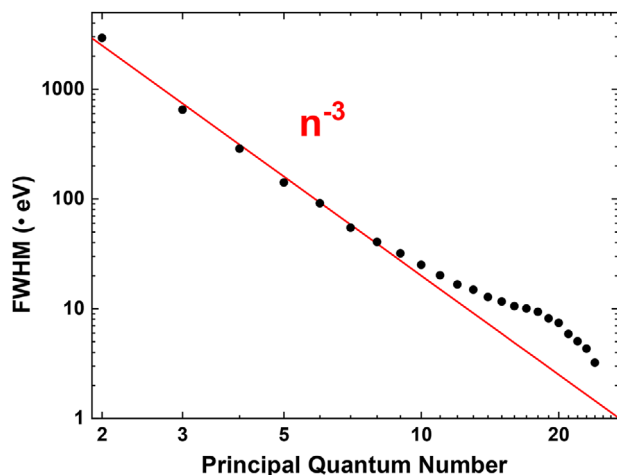


Figure 15. Scaling of the Rydberg exciton linewidth with n . Up to intermediate $n \approx 10$ the scaling follows the n^{-3} dependence known from atoms. For larger n a slight increase of the linewidth becomes apparent, which is usually interpreted as spectral broadening due to the presence of impurities and the presence of a second continuous phonon background to the 1S-exciton of the green series in this spectral range. Adapted with permission.^[6] Copyright 2014, Springer Nature.

be taken into account, which results in a significant energy shift. Further contributions to this deviation in binding energy arise due to the momentum dependence of the dielectric function and the coupling of LO phonons to electrons and holes.^[23]

Along with the binding energies, also the linewidths of the Rydberg exciton states are expected to scale with n . Here, considering only radiative recombination one expects a scaling law that goes as n^{-3} . Contributions due to phonon scattering are expected to show the same scaling.^[31] The experimentally determined linewidths of the Rydberg exciton states are shown in **Figure 15**.

As it turns out, the spectral widths of the low-lying states up to $n \approx 10$ match the n^{-3} scaling well, while there are significant deviations for larger n , which again become less pronounced for $n \approx 20$ and above. This deviation is usually interpreted as a

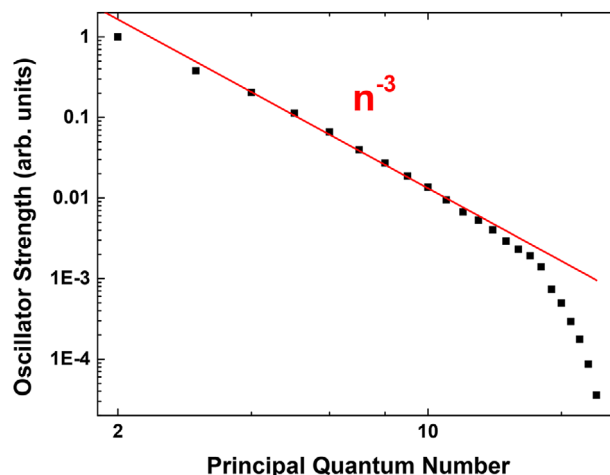


Figure 16. Scaling of the Rydberg exciton oscillator strength with n for a pump intensity of $6 \mu\text{W mm}^{-2}$, where blockade is already relevant for $n \geq 15$. Below the region, where blockade is significant, the oscillator strength scales as n^{-3} . Adapted with permission.^[6] Copyright 2014, Springer Nature.

consequence of the semiconductor environment. First, any real crystal will necessarily include some number of impurities and exciton states will interact with them. Due to the high crystal quality of the samples investigated here, the defect density is quite small and the impurities may be considered as dilute. In this case, excitons of larger n will have an enhanced probability to intersect with them due to their larger spatial extension. Further, the spectral regions, where the broadening of the lines becomes prominent coincides with the region where the second continuous phonon background absorption to the 1S exciton of the green series shows a significant increase of oscillator strength. It is expected that the presence of this additional interaction channel yields a contribution to the linewidth of the Rydberg states. It is remarkable that the linewidth of the highly excited states of the Rydberg series may become rather narrow. For the highest quantum numbers, linewidths of the order of few μeV are reached, which are determined by phonon scattering and radiative decay. The linewidth data therefore imply radiative lifetimes up to at least the nanosecond range.

Further, also the oscillator strength of the resonances is expected to scale with the principal quantum number. Although the increased radius of Rydberg states with large n implies that the dipole moments of these states increase drastically compared to the ground state, the reduced overlap between electron and hole and the narrow linewidths actually result in lower oscillator strength of Rydberg exciton states as compared to states with low n . The oscillator strengths for several states are shown in **Figure 16**.

For low principal quantum numbers, the oscillator strength of the resonances shows the n^{-3} scaling behavior known from Rydberg atoms. For large n , a clear deviation from this scaling law is apparent. The oscillator strength shows a much stronger reduction for $n \geq 15$. This is a consequence of the blockade effects discussed in the previous sections becoming important. As blockade sets in, the oscillator strengths at the peaks of the resonances get redistributed to other energies and forms a rather

broad background. The onset of these deviations does not occur at a fixed principal quantum number, but depends strongly on the applied pump power. Accordingly, this sudden change of oscillator strength scaling opens up another possibility to identify pump-dependent blockade effects.

These are only the most basic scaling laws occurring in Rydberg exciton systems. A lot of different scaling laws exist, especially in the presence of external fields. A detailed overview may be found elsewhere.^[62] Many scaling laws turn out to be similar to those for atoms. However, it should be pointed out that still the origin may be different. This is especially the case for scaling laws that originate from symmetry breaking and therefore quantum defects. For Rydberg atoms, the quantum defect arises due to screening by core carriers for all Rydberg atoms that are not hydrogen, which results in deviations from an ideal r^{-1} -potential. For Rydberg excitons, these deviations are indeed dominated by the non-parabolicity of the underlying valence bands, which also causes a quantum defect and scaling laws in close analogy to Rydberg atoms, although the origin of the quantum defect is very different. Here, it should be emphasized that the quantum defect is an important parameter in Rydberg physics that, for example, directly manifests as a phase shift of Rydberg atom wavefunctions,^[1] while it has usually been used in semiconductor physics only as a phenomenological parameter. These two meanings should not be confused and it is the former meaning from Rydberg atom physics, which is relevant for Rydberg excitons as well.

6. Energy Level Scheme

Quantum technologies based on Rydberg atoms are based heavily on the huge number of different states with different properties that Rydberg systems offer. Depending on the intended application, an experimentalist may choose a set of states tailored to the requirements of that application to work with. The lifetime of these states may be long or short. They may be coupled to other states forming a lambda, ladder, or vee scheme and optical transitions between several states may be possible with vastly differing transition probabilities and selection rules. Although optical transitions between different Rydberg states are not as important for Rydberg excitons because most transition frequencies are in the experimentally challenging THz-range, it is still mandatory to gather a comprehensive list of the states in the Rydberg exciton system to gain deeper insights into the Rydberg exciton level scheme. As the spectral separations between the states are much smaller compared to atomic systems, many of them may contribute to resonant or non-resonant interactions, especially in the presence of external fields. In this section we will discuss the energy levels of Rydberg exciton states of the yellow series in Cu_2O that have already been observed experimentally and how to determine their energies. A full summary of all states of the yellow series observed in experiments so far, is shown in **Figure 17**. Information about other levels may be found elsewhere.^[25,59,66]

The most easily accessible Rydberg exciton states in Cu_2O are the *P*-excitons. Transitions to these states are dipole-allowed and they have been observed directly in transmission measurements for principal quantum numbers between $n = 2$ and 28.^[6] Due to optical selection rules, these should be the only discrete Rydberg

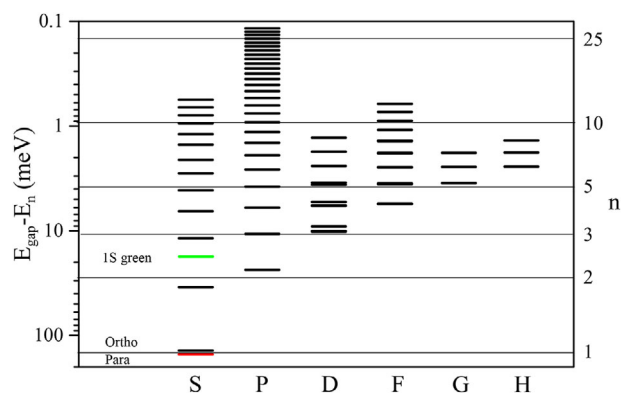


Figure 17. Scheme of experimentally observed Rydberg orthoexciton states of the yellow series. For comparison, the yellow 15 paraexciton is shown in red and the green 1S state is shown in green.

exciton states showing up as dipole transitions in optical transmission spectra, using the spherical approximation. However, the system, in which the excitons reside is a Cu_2O semiconductor crystal that necessarily shows reduced symmetry compared to individual atoms in vacuum. For hydrogen the spatial symmetry is given by the continuous rotation group $\text{SO}(3)$, which implies that the squared orbital angular momentum $L^2 = l(l+1)\hbar^2$ and the magnetic quantum number m are constants of motion. Further, the r^{-1} dependence of the Coulomb potential corresponds to $\text{SO}(4)$ symmetry. The latter symmetry causes energy levels of different l to be degenerate, while the former results in degeneracy of energy levels of different m . Inside a semiconductor crystal, the continuous rotational symmetry is reduced to a discrete rotational symmetry (symmetry group O_h) by the presence of the lattice. Accordingly, l and m are strictly speaking not good quantum numbers anymore. It is known that a significant reduction of the symmetry of a system, for example, by applying external fields to (low-dimensional) semiconductor systems,^[67,68] allows one to observe exciton states of different orbital angular momentum. However, in most bulk materials the mere presence of the lattice is not sufficient to result in an observable lifting of the degeneracy with respect to l and m . In Cu_2O , the large exciton binding energy and narrow linewidths make it possible to observe the influence of the lattice on the system symmetry directly via the appearance of higher angular momentum states that have the same parity as *P*-excitons.^[55] An experimental spectrum that shows *F*-excitons—or rather states of mixed *P*- and *F*-character—for $n \geq 4$ is shown in **Figure 18**. As the largest value of l that may appear for a given principal quantum number is $n - 1$, $n = 4$ is also the first state for which *F*-excitons are expected to be observable. These states show a threefold splitting as expected from theory. A closer look even reveals the appearance of *H*-excitons for $n \geq 6$. In order to investigate the fine structure for states of given l in even more detail, one may additionally apply magnetic fields.^[69–73]

Observation of the exciton states with even l are non-trivial as optical transitions to these states are not dipole-allowed due to parity. Accordingly, there are two standard ways to investigate these states by optical means. First, one may introduce odd-parity perturbations that mix exciton states of odd and even parity. Due to the mixing with dipole-allowed exciton states, the even-parity states will gain some oscillator strength and undergo an energy

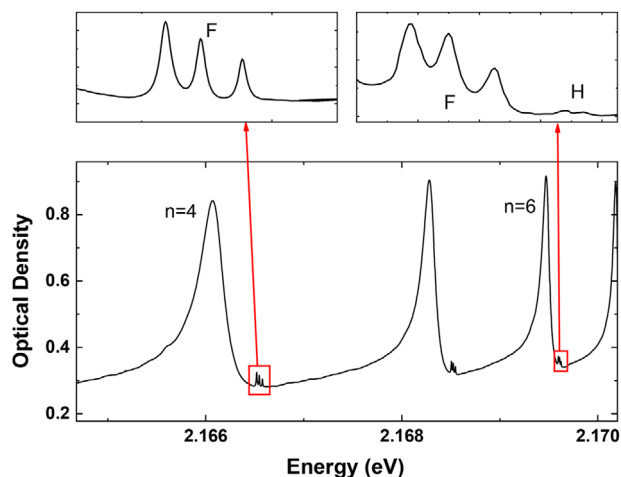


Figure 18. Rydberg exciton spectrum in the region between $n = 4$ and $n = 6$. The top panels show close-ups of the high energy sides of the $n = 4$ and $n = 6$ resonances, where F - and H -exciton states appear. The spectra also show a clear energy splitting of the F -exciton states. Adapted with permission.^[55] Copyright 2015, American Physical Society.

shift depending on the magnitude of the perturbation. Plotting this energy shift against the magnitude of the perturbation and extrapolating the results toward a vanishing perturbation strength yields the energies of the unperturbed even-parity resonances. A prime candidate for such an odd-parity perturbation is an external electric field.^[51,52,62] Alternatively, one may avoid the parity problem by using optical processes with different selection rules. Especially high-resolution second-harmonic spectroscopy is a good approach.^[74]

Second harmonic generation (SHG) is a coherent process in which an optical transition at energy $\hbar\omega$ is excited by two photons, each having half the energy of the transition. This excitation process creates an electronic polarization which subsequently emits radiation with frequency ω if allowed by the selection rules. The remarkable coherence of the exciton states in cuprous oxide asks for studying them by SHG. Obviously, the SHG selection rules are expected to be different from those in linear spectroscopy such as transmission or absorption. One therefore can expect to observe in SHG exciton states different from those observed in one-photon processes. This potential can be used to combine linear and non-linear spectroscopy to develop a detailed picture of the exciton series and, as we will see, study light-matter interaction processes at an unprecedented level in semiconductors, where one often can restrict to the electric dipole approximation.

As described before, the exciton states that are observed in transmission are dominantly P -excitons of odd symmetry as well as other odd excitons with F, H, \dots envelope functions due to their mixing with the P -excitons by the crystal environment. This restriction arises from the odd symmetry of the electric dipole operator. Restricting to the dipole approximation, one expects that P -excitons cannot be excited in a two-photon transition. Instead, excitons of even symmetry such as S, D, \dots states might be excitable. However, SHG requires subsequent emission of a photon, which is forbidden for these states in dipole approximation.

Figure 19 shows SHG spectra of a thin cuprous oxide crystal oriented such that the optical axis is along the $[111]$ crystal direction. For comparison, the black lines show the linear transmission spectra.^[74] In the energy range of the $n = 3$ exciton multiplet, one observes two intense SHG lines, one at the low energy flank of the $3P$ exciton, the other one on the high energy flank. Also by comparing the energies with the results of detailed calculations,^[70] we tentatively assign the two SHG lines to the $3S$ and $3D$ excitons. In the spectral ranges of the $n = 5$ and $n = 6$ multiplets one observes the same signatures with two dominating SHG lines enclosing the associated P -exciton, see the right panel. In analogy we assign also here the two SHG lines to S and D excitons, respectively, which are mixed by the crystal structure.

While two-photon excitation of the even excitons is allowed according to the considerations above, the SHG photon emission mechanism is surprising. As dipole emission is forbidden, this requires involvement of a high order process and it is tempting to assign the emission to the next higher order of a quadrupole process. As shown in **Figure 20**, the three-photon SHG process involving the even excitons would then involve two dipole transitions in the excitation and the quadrupole transition in the deexcitation which can be tested by measuring rotational anisotropies: In such a measurement of the SHG intensity, the relative linear polarizations of the fundamental, and the SHG light are fixed and synchronously varied in a continuous fashion. The expected variation of the SHG intensity can be easily calculated from a group theory-based symmetry analysis accounting for the experimental configuration, the crystal symmetry and the transition operators. Compared to atoms, such measurements are easily performed due to the fixed relative orientations of the exciting/emitted light and the involved copper atomic orbitals.

Figure 21, bottom left, shows a polar plot of the SHG intensity calculated for an even exciton with the light wave vector along the $[11\bar{2}]$ crystal direction. The black (red) shaded area gives the results for parallel (perpendicular) relative polarizations, revealing characteristic variations when varying the polarization. For parallel orientation, four directions with strong SHG intensity are seen, while for perpendicular orientation mainly only two strong directions different from the other configuration exist. **Figure 21**, top left, shows the corresponding experimental data recorded on the $3S$ exciton with the optical axis along the $[11\bar{2}]$ -direction, which are in good accord with the expectation, except for some distortion which may be due to some slight misalignment or some strain in the sample. However, in the perpendicular configuration even the four directions with rather weak SHG intensity are resolved. The good overall agreement between theory and experiment confirms the suggested microscopic mechanism for SHG on even excitons.

Coming back to the spectra, one notes that in between the two strong SHG features for a particular n , there is another rather weak one as can be seen for $n = 6$ in **Figure 19**. Its energy coincides well with that of the associated P -exciton, so that rather surprisingly SHG is generated also on odd excitons, which cannot be excited by two dipole transitions, but can emit a photon in this order. This may be explained by exchanging the role of the dipole and the quadrupole transition in the SHG process on the even excitons, so that excitation is arranged by combining a dipole and a quadrupole transition, exciting the odd exciton, followed by dipolar emission, as sketched in the right panel of **Figure 20**. Again,

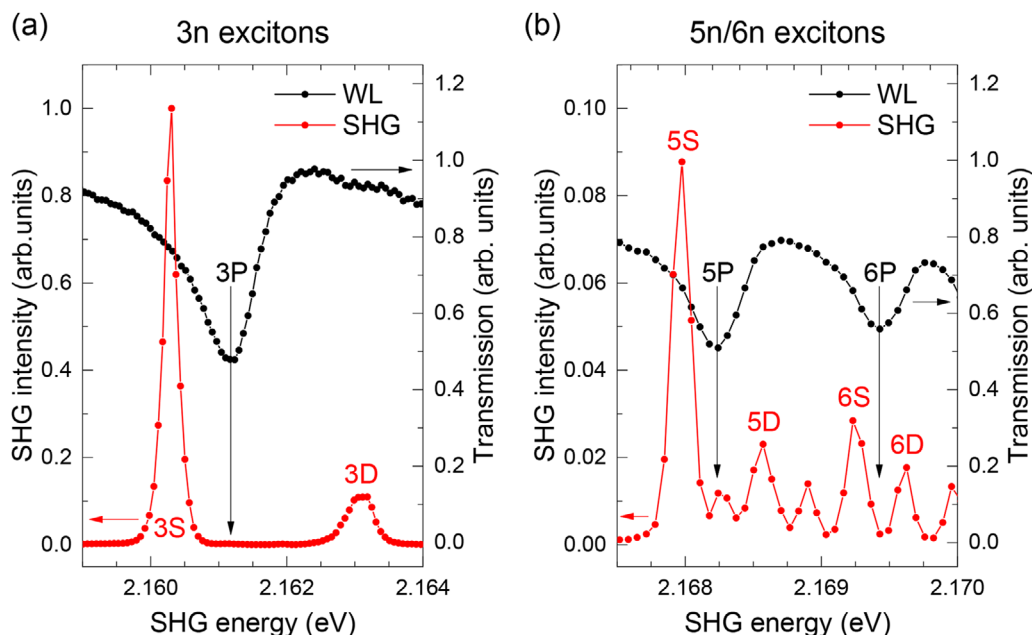


Figure 19. SHG spectra (red traces) in the spectral range of the $n = 3$ exciton (left) and the $n = 5$ and 6 excitons (right).^[74] Excitation was performed with a laser emitting 200 fs pulses with the central photon energy of the fundamental light at 1.017 eV. The emission in the spectral range around twice this photon energy is dispersed by a monochromator and detected by a CCD-camera. The spectra were recorded for parallel linear polarization of the fundamental and the SHG light along the $[11\bar{2}]$ crystal direction. The black traces give the corresponding linear white light (WL) transmission spectra which are dominated by the P -exciton resonances. Adapted with permission.^[74] Copyright 2018, American Physical Society.

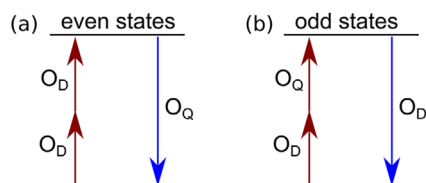


Figure 20. Sketches of the SHG process on the even (left) and (odd) excitons in cuprous oxide. Reproduced with permission.^[74] Copyright 2018, American Physical Society.

this assumption can be justified by calculating and measuring the rotational SHG anisotropies, shown in Figure 21, right column. The experimental data were taken on the $2P$ exciton with the light propagating along the $[111]$ -direction, and correspond in both polarization configurations with a characteristic antiphase behavior to the calculations, providing a powerful proof of the quadrupole-dipole and dipole sequence in the SHG process.

These results underline that it is possible to excite particular exciton states by one- or two-photon processes. These possibilities are even more extended by applying external fields. Again we have tested this by SHG spectroscopy, for which we have chosen the optical axis to be parallel to the $[1\bar{1}0]$ direction, along which no SHG is generated without magnetic field for symmetry reasons. Applying a magnetic field in Voigt configuration along the $[110]$ crystal direction induces strong SHG signal, as can be seen from the spectra in Figure 22,^[75,76] where the linear polarization of the fundamental light is chosen to be along the field and the polarization of the SHG light is rotated by 45° relative to it. The signal increases strongly with magnetic field and involves all states within a multiplet.

The origin of this signal is the so-called magneto-Stark-effect, which is particularly pronounced for excitons compared to atoms due to their much smaller effective mass.^[77] Namely, the sum of the momenta of the two exciting photons is transferred onto the center-of-mass motion of the excitons, which in Voigt-configuration is normal to the magnetic field. Thus the constituting electron and hole of the exciton experience Lorentz forces in opposite directions, so that the exciton becomes polarized like in an electric field. The effect can indeed be mapped onto an effective electric field \mathbf{F} , which is given by

$$\mathbf{F} = \frac{\hbar e}{M}(\mathbf{K} \times \mathbf{B}), \quad (24)$$

where the term in bracket is the cross product of the exciton momentum \mathbf{K} and the magnetic field \mathbf{B} , \hbar is the Planck constant, e is the elementary charge, and M is the exciton mass. The effect of this “effective” electric field with odd parity is a mixing of even and odd exciton states, making SHG allowed for basically all states within an exciton multiplet. Vice versa, this shows that tailored exciton superpositions composed of S -, P -, D -, ... states can be excited optically with the mixing controlled by the orientation and strength of the applied magnetic field or by an (additional) electric field.

7. Outlook

The purpose of this review article is to discuss the specific properties of semiconductor Rydberg systems with respect to their atomic counterparts and to highlight both the fundamental

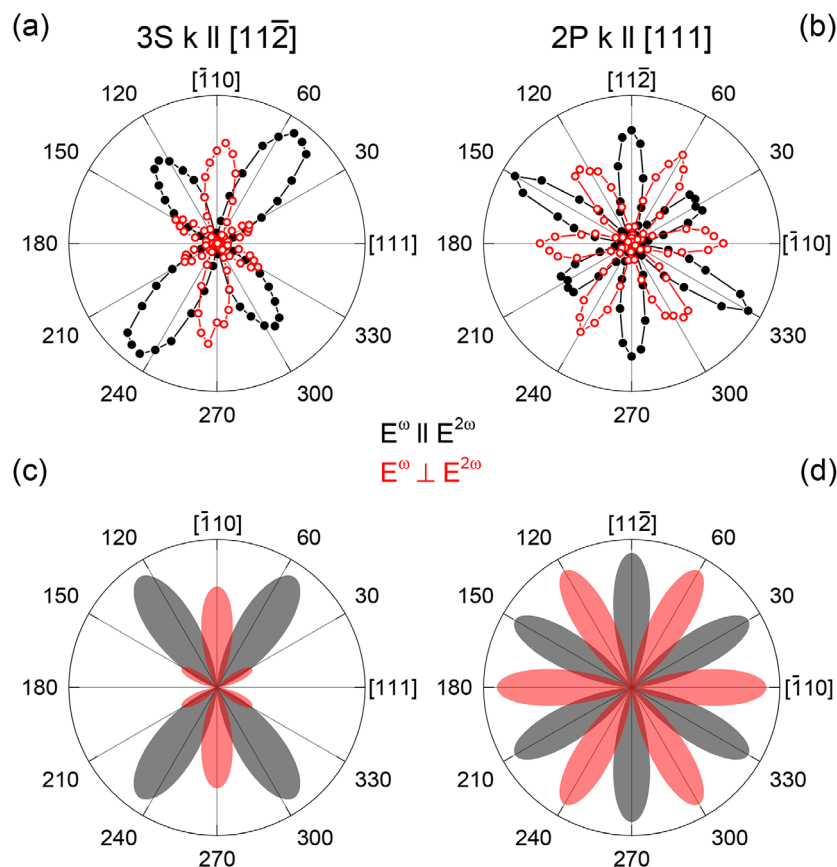


Figure 21. Polar plots of the SHG intensity as function of the linear polarization angle of the fundamental light with the SHG polarization parallel (black shaded areas) or perpendicular to it (red shaded areas). The lower row shows simulations for the even (left) and the odd (right) excitons, the upper row experimental data recorded on the 3S (left) and the 2P (right) exciton. Adapted with permission.^[74] Copyright 2018, American Physical Society.

similarities and differences. While both systems show Rydberg blockade effects, their physical properties and therefore also the potential range of applications they are suitable for, are very different. Cold atoms are stable particles that may be placed at well defined positions and that have well separated states. This renders them ideal building blocks for realizing quantum technologies that rely on precise positioning or long-term stability of the system properties such as quantum computing in optical lattices or electromagnetic field sensing.^[78] Excitons on the other hand are subject to collective excitations of their semiconductor host material and are transient particles that may decay and be created again. The semiconductor environment and the typical time and energy scales involved render them ideal for high speed applications or for interfaces between photonics and semiconductor physics. In fact, already a significant number of possible applications and quantum technologies based on Rydberg excitons has been proposed: It has been suggested that microcavities may help to enhance optical nonlinearities by several orders of magnitude, if the problem of phonon-based loss channels is overcome,^[79] which may pave a way towards nonlinearities on the single photon level. Also, the radiative coupling in Cu₂O seems to be highly size-dependent,^[80] so microcrystals^[81] or low-dimensional nanostructures such as quantum dots,^[82] quantum wires^[83] and quantum wells^[84] seem like ideal candidates for tailoring the optical properties of quantum technologies based

on Cu₂O. So far the technology for fabrication and patterning of Cu₂O is still in its infancy, and is also challenging because the material is rather brittle. On the other hand, also protocols for Rydberg exciton blockade-based single photon sources at high repetition rates have been presented^[85] as well as ideas to incorporate Rydberg excitons in traditional devices such as masers.^[86,87] Recently, also the possibility to utilize the high tunability of the Rydberg exciton platform to observe non-trivial topological Haldane phases in Cu₂O has been discussed.^[88]

Also from a more elemental point of view, Rydberg excitons bear the potential for new groundbreaking insights into fundamental physics. Their large spatial extent makes them an ideal testbed for spectroscopy using spatially tailored light fields, which has proven to be a successful approach to tailor the properties of other spatially extended systems.^[89,90] For example, it has been predicted that excitation using twisted light will modify the selection rules in optical transitions significantly.^[21] Further, Rydberg excitons are an ideal testbed to study the effects of quantum chaos^[91–95] because for excitons the high-field regime, where quantum chaos is expected to set in, is reached already at moderate magnetic fields that can be realized easily in a lab setting. It is expected that Rydberg excitons are a rare instance of an atom-like system^[96] that shows quantum chaos and exceptional points.^[97,98] The latter are usually found only in especially engineered billiard resonators.^[99–101] It has been pointed out that

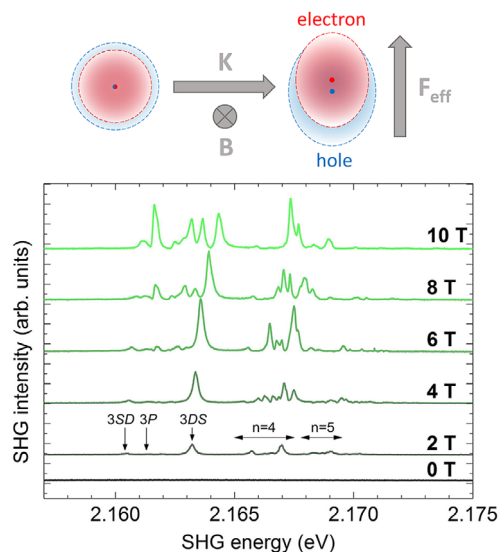


Figure 22. SHG induced by application of a magnetic field: the bottom panel shows spectra recorded in a magnetic field from zero up to 10 T, applied in the Voigt configuration with $B \parallel [110]$ and the fundamental light wave vector $k \parallel [1\bar{1}0]$. The linear polarization of the fundamental light is chosen to be parallel to B , the polarization of the SHG light is rotated by 45° relative to this direction. The displayed energy range covers mostly excitons with $n = 3, 4, 5$. The signal is induced by the magneto-Stark-effect, which is explained in the sketch. Adapted with permission.^[75] Copyright 2020, American Physical Society.

exceptional points are very beneficial for precision and quantum sensing under some circumstances.^[102,103] Therefore, the discovery of exceptional points in the level spectrum of Cu_2O would be an important discovery.

Rydberg excitons provide a highly versatile, tunable, and scalable platform for various quantum technologies and applications in quantum sensing and imaging. However, as the field is developing quickly, especially in terms of the available materials and the technology to process them, the potential applications and research directions outlined above are only a first step and it is very likely that additional unforeseen technological breakthroughs and fundamental discoveries will be added to the list.

Acknowledgements

The authors thank the Dortmund team that was involved in reaching the level of understanding presented above, namely (in alphabetical order): A. Farenbruch, M. Freitag, J. Heckötter, J. Mund, T. Kazimierczuk, D.R. Yakovlev, and in particular D. Fröhlich.

The authors also thank their theoretical collaborators: M. Semina and M. Glazov from the Ioffe-Institute in St. Petersburg; P. Rommel, F. Schweiner, G. Wunner and J. Main from the University Stuttgart; P. Grünwald, S.O. Krüger, D. Semkat, H. Stolz, and S. Scheel from the University Rostock; V. Walther and Th. Pohl from the University Aarhus.

The authors gratefully acknowledge funding by the Deutsche Forschungsgemeinschaft (DFG, German Research Foundation) via TRR 160 in the project A8 and the project Hocharaufgelöste Spektroskopie an Rydbergexzitonen in äußeren Feldern.

Conflict of Interest

The authors declare no conflict of interest.

Keywords

cuprous oxide, laser spectroscopy, Rydberg excitons, semiconductors

Received: December 6, 2019

Revised: March 25, 2020

Published online: June 8, 2020

- [1] T. F. Gallagher, *Rydberg Atoms*, Cambridge Monographs on Atomic Physics. Cambridge University Press, Cambridge **2005**.
- [2] M. Saffman, T. G. Walker, K. Mølmer, *Rev. Mod. Phys.* **2010**, *82*, 2313.
- [3] J. A. Sedlacek, A. Schwettmann, H. Kübler, R. Löw, T. Pfau, J. P. Shaffer, *Nat. Phys.* **2012**, *8*, 819.
- [4] C. G. Wade, N. Sibalic, N. R. de Melo, J. M. Kondo, C. S. Adams, K. J. Weatherill, *Nat. Photonics* **2016**, *11*, 40.
- [5] L. A. Downes, A. R. MacKellar, D. J. Whiting, C. Bourgenot, C. S. Adams, K. J. Weatherill, *Phys. Rev. X* **2020**, *10*, 011027.
- [6] T. Kazimierczuk, D. Fröhlich, S. Scheel, H. Stolz, M. Bayer, *Nature* **2014**, *514*, 343.
- [7] A. J. Ångström, *Recherches sur le spectre solaire*, Uppsala, W. Schultz, **1868**.
- [8] J. J. Balmer, *Annalen der Physik* **1885**, *261*, 80.
- [9] J. R. Rydberg, *London, Edinburgh Dublin Philos. Mag. J. Sci.* **1890**, *29*, 331.
- [10] N. Šibalić, C. S. Adams, *Rydberg Physics*, IOP Publishing, Bristol, UK **2018**.
- [11] K. Singer, J. Stanojevic, M. Weidemüller, R. Côté, *J. Phys. B: At., Mol. Opt. Phys.* **2005**, *38*, S295.
- [12] C. L. Vaillant, M. P. A. Jones, R. M. Potvliege, *J. Phys. B: At., Mol. Opt. Phys.* **2012**, *45*, 135004.
- [13] A. Reinhard, T. C. Liebisch, B. Knuffman, G. Raithe, *Phys. Rev. A* **2007**, *75*, 032712.
- [14] S. Weber, C. Tresp, H. Menke, A. Urvoy, O. Firstenberg, H. P. Büchler, S. Hofferberth, *J. Phys. B: At., Mol. Opt. Phys.* **2017**, *50*, 133001.
- [15] N. Šibalić, J. Pritchard, C. Adams, K. Weatherill, *Comput. Phys. Commun.* **2017**, *220*, 319.
- [16] D. Jaksch, J. I. Cirac, P. Zoller, S. L. Rolston, R. Côté, M. D. Lukin, *Phys. Rev. Lett.* **2000**, *85*, 2208.
- [17] M. D. Lukin, M. Fleischhauer, R. Cote, L. M. Duan, D. Jaksch, J. I. Cirac, P. Zoller, *Phys. Rev. Lett.* **2001**, *87*, 037901.
- [18] A. Chernikov, T. C. Berkelbach, H. M. Hill, A. Rigosi, Y. Li, O. B. Aslan, D. R. Reichman, M. S. Hybertsen, T. F. Heinz, *Phys. Rev. Lett.* **2014**, *113*, 076802.
- [19] G. F. Koster, J. O. Dimmock, R. G. Wheeler, H. Statz, *Properties of the Thirty-Two Point Groups*, The MIT Press, Cambridge, MA **1963**.
- [20] R. J. Elliott, *Phys. Rev.* **1961**, *124*, 340.
- [21] A. M. Konzelmann, S. O. Krüger, H. Giessen, *Phys. Rev. B* **2019**, *100*, 115308.
- [22] M. A. Washington, A. Z. Genack, H. Z. Cummins, R. H. Bruce, A. Compaan, R. A. Forman, *Phys. Rev. B* **1977**, *15*, 2145.
- [23] G. M. Kavoulakis, Y.-C. Chang, G. Baym, *Phys. Rev. B* **1997**, *55*, 7593.
- [24] F. Schöne, S.-O. Krüger, P. Grünwald, H. Stolz, S. Scheel, M. Aßmann, J. Heckötter, J. Thewes, D. Fröhlich, M. Bayer, *Phys. Rev. B* **2016**, *93*, 075203.
- [25] F. Schweiner, J. Main, G. Wunner, C. Uihlein, *Phys. Rev. B* **2017**, *95*, 195201.
- [26] J. Brandt, D. Fröhlich, C. Sandfort, M. Bayer, H. Stolz, N. Naka, *Phys. Rev. Lett.* **2007**, *99*, 217403.
- [27] R. Forman, W. Brower, H. Parker, *Phys. Lett. A* **1971**, *36*, 395.
- [28] F. Schöne, H. Stolz, N. Naka, *Phys. Rev. B* **2017**, *96*, 115207.
- [29] Y. Toyozawa, *J. Phys. Chem. Solids* **1964**, *25*, 59.
- [30] S. Zielińska-Raczyńska, G. Czajkowski, D. Ziemkiewicz, *Phys. Rev. B* **2016**, *93*, 075206.

- [31] H. Stolz, F. Schöne, D. Semkat, *New J. Phys.* **2018**, *20*, 023019.
- [32] W. C. Tait, *Phys. Rev. B* **1972**, *5*, 648.
- [33] D. Fröhlich, A. Kulik, B. Uebbing, A. Mysyrowicz, V. Langer, H. Stolz, W. von der Osten, *Phys. Rev. Lett.* **1991**, *67*, 2343.
- [34] J. Schmutzler, D. Fröhlich, M. Bayer, *Phys. Rev. B* **2013**, *87*, 245202.
- [35] S. Zielińska-Raczyńska, G. Czajkowski, K. Karpiński, D. Ziemkiewicz, *Phys. Rev. B* **2019**, *99*, 245206.
- [36] S. Zielińska-Raczyńska, D. Ziemkiewicz, G. Czajkowski, *Phys. Rev. B* **2018**, *97*, 165205.
- [37] N. F. Mott, *Rev. Mod. Phys.* **1968**, *40*, 677.
- [38] J. Collet, *J. Phys. Chem. Solids* **1985**, *46*, 417.
- [39] M. Capizzi, S. Modesti, A. Frova, J. L. Staehli, M. Guzzi, R. A. Logan, *Phys. Rev. B* **1984**, *29*, 2028.
- [40] G. B. Norris, K. K. Bajaj, *Phys. Rev. B* **1982**, *26*, 6706.
- [41] G. W. Fehrenbach, W. Schäfer, J. Treusch, R. G. Ulbrich, *Phys. Rev. Lett.* **1982**, *49*, 1281.
- [42] K. Yao, A. Yan, S. Kahn, A. Suslu, Y. Liang, E. S. Barnard, S. Tongay, A. Zettl, N. J. Borys, P. J. Schuck, *Phys. Rev. Lett.* **2017**, *119*, 087401.
- [43] R. Zimmermann, *Phys. Status Solidi B* **1988**, *146*, 371.
- [44] D. Semkat, F. Richter, D. Kremp, G. Manzke, W.-D. Kraeft, K. Henneberger, *Phys. Rev. B* **2009**, *80*, 155201.
- [45] F. Liu, M. E. Ziffer, K. R. Hansen, J. Wang, X. Zhu, *Phys. Rev. Lett.* **2019**, *122*, 246803.
- [46] J. Heckötter, M. Freitag, D. Fröhlich, M. Aßmann, M. Bayer, P. Grünwald, F. Schöne, D. Semkat, H. Stolz, S. Scheel, *Phys. Rev. Lett.* **2018**, *121*, 097401.
- [47] J. Seidel, S. Arndt, W. D. Kraeft, *Phys. Rev. E* **1995**, *52*, 5387.
- [48] S. Paul, Y. K. Ho, *Phys. Plasmas* **2009**, *16*, 063302.
- [49] P. Grünwald, M. Aßmann, J. Heckötter, D. Fröhlich, M. Bayer, H. Stolz, S. Scheel, *Phys. Rev. Lett.* **2016**, *117*, 133003.
- [50] D. Semkat, H. Fehske, H. Stolz, *Phys. Rev. B* **2019**, *100*, 155204.
- [51] J. Heckötter, M. Freitag, D. Fröhlich, M. Aßmann, M. Bayer, M. A. Semina, M. M. Glazov, *Phys. Rev. B* **2017**, *95*, 035210.
- [52] J. Heckötter, M. Freitag, D. Fröhlich, M. Aßmann, M. Bayer, M. A. Semina, M. M. Glazov, *Phys. Rev. B* **2018**, *98*, 035150.
- [53] C. Ciuti, V. Savona, C. Piermarocchi, A. Quattropani, P. Schwendimann, *Phys. Rev. B* **1998**, *58*, 7926.
- [54] V. Walther, S. O. Krüger, S. Scheel, T. Pohl, *Phys. Rev. B* **2018**, *98*, 165201.
- [55] J. Thewes, J. Heckötter, T. Kazimierczuk, M. Aßmann, D. Fröhlich, M. Bayer, M. A. Semina, M. M. Glazov, *Phys. Rev. Lett.* **2015**, *115*, 027402.
- [56] H. Tanimura, K. Tanimura, P. H. M. van Loosdrecht, *Phys. Rev. B* **2019**, *100*, 115204.
- [57] A. Mysyrowicz, D. Hulin, C. B. A. L. Guillaume, *J. Lumin.* **1981**, *24-25*, 629.
- [58] J. T. Warren, K. E. O'Hara, J. P. Wolfe, *Phys. Rev. B* **2000**, *61*, 8215.
- [59] M. Takahata, N. Naka, *Phys. Rev. B* **2018**, *98*, 195205.
- [60] T. Kitamura, M. Takahata, N. Naka, *J. Lumin.* **2017**, *192*, 808.
- [61] M. Kubouchi, K. Yoshioka, R. Shimano, A. Mysyrowicz, M. Kawata-Gonokami, *Phys. Rev. Lett.* **2005**, *94*, 016403.
- [62] J. Heckötter, M. Freitag, D. Fröhlich, M. Aßmann, M. Bayer, M. A. Semina, M. M. Glazov, *Phys. Rev. B* **2017**, *96*, 125142.
- [63] D. Fröhlich, R. Kenkies, C. Uihlein, C. Schwab, *Phys. Rev. Lett.* **1979**, *43*, 1260.
- [64] F. Schöne, S.-O. Krüger, P. Grünwald, M. Aßmann, J. Heckötter, J. Thewes, H. Stolz, D. Fröhlich, M. Bayer, S. Scheel, *J. Phys. B: At. Mol. Opt. Phys.* **2016**, *49*, 134003.
- [65] J. Heckötter, J. Thewes, D. Fröhlich, M. Aßmann, M. Bayer, *Phys. Solid State* **2018**, *60*, 1625.
- [66] S. O. Krüger, S. Scheel, *Phys. Rev. B* **2019**, *100*, 085201.
- [67] L. Viña, G. E. W. Bauer, M. Potemski, J. C. Maan, E. E. Mendez, W. I. Wang, *Phys. Rev. B* **1988**, *38*, 10154.
- [68] L. Viña, G. E. W. Bauer, M. Potemski, J. C. Maan, E. E. Mendez, W. I. Wang, *Phys. Rev. B* **1990**, *41*, 10767.
- [69] S. Artyukhin, D. Fishman, C. Faugeras, M. Potemski, A. Revcolevschi, M. Mostovoy, P. H. M. v. Loosdrecht, *Sci. Rep.* **2018**, *8*, 7818.
- [70] F. Schweiner, J. Main, G. Wunner, M. Freitag, J. Heckötter, C. Uihlein, M. Aßmann, D. Fröhlich, M. Bayer, *Phys. Rev. B* **2017**, *95*, 035202.
- [71] S. Zielińska-Raczyńska, D. Ziemkiewicz, G. Czajkowski, *Phys. Rev. B* **2016**, *94*, 045205.
- [72] S. Zielińska-Raczyńska, D. Ziemkiewicz, G. Czajkowski, *Phys. Rev. B* **2017**, *95*, 075204.
- [73] S. Zielińska-Raczyńska, D. A. Fishman, C. Faugeras, M. M. P. Potemski, P. H. M. van Loosdrecht, K. Karpiński, G. Czajkowski, D. Ziemkiewicz, *New J. Phys.* **2019**, *21*, 103012.
- [74] J. Mund, D. Fröhlich, D. R. Yakovlev, M. Bayer, *Phys. Rev. B* **2018**, *98*, 085203.
- [75] A. Farenbruch, J. Mund, D. Fröhlich, D. R. Yakovlev, M. Bayer, M. A. Semina, M. M. Glazov, *Phys. Rev. B* **2020**, *101*, 115201.
- [76] P. Rommel, J. Main, A. Farenbruch, J. Mund, D. Fröhlich, D. R. Yakovlev, M. Bayer, C. Uihlein, *Phys. Rev. B* **2020**, *101*, 115202.
- [77] P. Rommel, F. Schweiner, J. Main, J. Heckötter, M. Freitag, D. Fröhlich, K. Lehninger, M. Aßmann, M. Bayer, *Phys. Rev. B* **2018**, *98*, 085206.
- [78] C. S. Adams, J. D. Pritchard, J. P. Shaffer, *J. Phys. B: At., Mol. Opt. Phys.* **2019**.
- [79] V. Walther, R. John, T. Pohl, *Nat. Commun.* **2018**, *9*, 1309.
- [80] M. Takahata, K. Tanaka, N. Naka, *Phys. Rev. B* **2018**, *97*, 205305.
- [81] S. Steinhauer, M. A. M. Versteegh, S. Gyger, A. W. Elshaari, B. Kunert, A. Mysyrowicz, V. Zwiller, *Commun. Mater.* **2020**, *1*, 11.
- [82] M. Y. Lee, S.-H. Kim, I.-K. Park, *Phys. B* **2016**, *500*, 4.
- [83] Y. Zhou, Y. Wang, Y. Guo, *Mater. Lett.* **2019**, *254*, 336.
- [84] A. Konzelmann, B. Frank, H. Giessen, *J. Phys. B: At., Mol. Opt. Phys.* **2019**, *53*, 024001.
- [85] M. Khazali, K. Heshami, C. Simon, *J. Phys. B: At., Mol. Opt. Phys.* **2017**, *50*, 215301.
- [86] D. Ziemkiewicz, S. Zielińska-Raczyńska, *Opt. Lett.* **2018**, *43*, 3742.
- [87] D. Ziemkiewicz, S. Zielińska-Raczyńska, *Opt. Express* **2019**, *27*, 16983.
- [88] A. N. Poddubny, M. M. Glazov, *Phys. Rev. Lett.* **2019**, *123*, 126801.
- [89] M. Aßmann, F. Veit, M. Bayer, A. Löffler, S. Höfling, M. Kamp, A. Forchel, *Phys. Rev. B* **2012**, *85*, 155320.
- [90] J. Schmutzler, P. Lewandowski, M. Aßmann, D. Niemietz, S. Schumacher, M. Kamp, C. Schneider, S. Höfling, M. Bayer, *Phys. Rev. B* **2015**, *91*, 195308.
- [91] F. Schweiner, J. Main, G. Wunner, *Phys. Rev. Lett.* **2017**, *118*, 046401.
- [92] M. Aßmann, J. Thewes, D. Fröhlich, M. Bayer, *Nat. Mater.* **2016**, *15*, 741.
- [93] F. Schweiner, J. Main, G. Wunner, *Phys. Rev. E* **2017**, *95*, 062205.
- [94] M. Freitag, J. Heckötter, M. Bayer, M. Aßmann, *Phys. Rev. B* **2017**, *95*, 155204.
- [95] F. Schweiner, P. Rommel, J. Main, G. Wunner, *Phys. Rev. B* **2017**, *96*, 035207.
- [96] A. Frisch, M. Mark, K. Aikawa, F. Ferlaino, J. L. Bohn, C. Makrides, A. Petrov, S. Kotochigova, *Nature* **2014**, *507*, 475.
- [97] H. Cartarius, J. Main, G. Wunner, *Phys. Rev. Lett.* **2007**, *99*, 173003.
- [98] M. Feldmaier, J. Main, F. Schweiner, H. Cartarius, G. Wunner, *J. Phys. B: At., Mol. Opt. Phys.* **2016**, *49*, 144002.
- [99] U. Stöckmann, J. Stein, H.-J. Stöckmann, M. Kuś, F. Haake, *Phys. Rev. Lett.* **1995**, *74*, 2666.
- [100] T. Gao, E. Estrecho, K. Y. Bliokh, T. C. H. Liew, M. D. Fraser, S. Brodbeck, M. Kamp, C. Schneider, S. Hofling, Y. Yamamoto, F. Nori, Y. S. Kivshar, A. G. Truscott, R. G. Dall, E. A. Ostrovskaya, *Nature* **2015**, *526*, 554.
- [101] L. A. Ponomarenko, F. Schedin, M. I. Katsnelson, R. Yang, E. W. Hill, K. S. Novoselov, A. K. Geim, *Science* **2008**, *320*, 356.
- [102] J. Wiersig, *Phys. Rev. A* **2016**, *93*, 033809.
- [103] W. Langbein, *Phys. Rev. A* **2018**, *98*, 023805.